Absorber and interfaces of kesterite solar cells

Siddhartha Garud

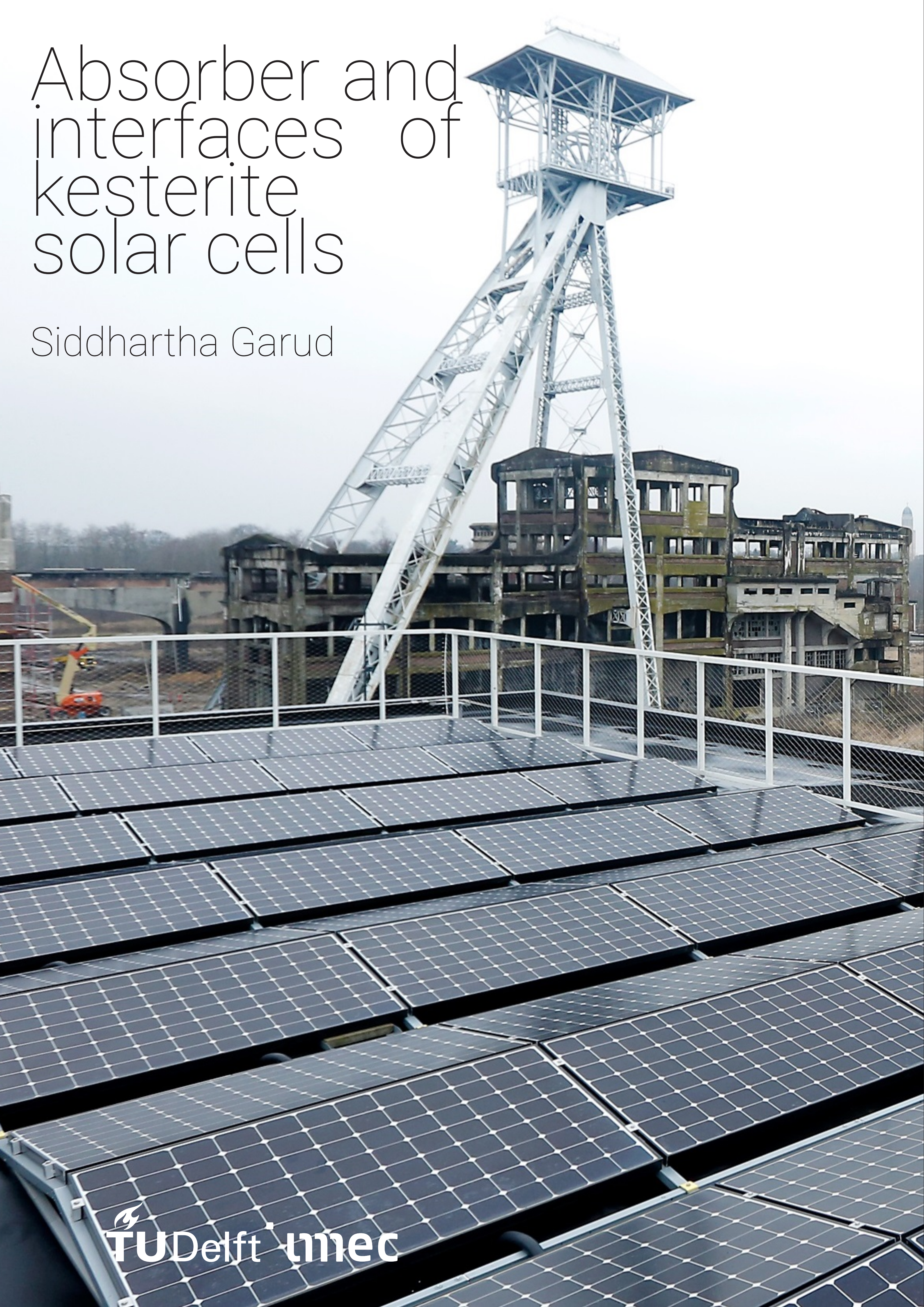

Absorber and interfaces of kesterite solar cells

by

Siddhartha Garud

in partial fulfillment of the requirements for the degree of

Master of Science

in Electrical Engineering,
under the faculty of Electrical Engineering, Mathematics and Computer Science,

at the Delft University of Technology,
to be defended publicly on Tuesday July 4, 2017 at 14:30 AM.

Student number:	4517644	
Project duration:	July 18, 2016 – June 30, 2017	
Thesis committee:	Prof. dr. ir. A.H.M. Smets,	TU Delft
	Prof. dr. Bart Vermang,	imec, Hasselt University
	Dr. Olindo Isabella,	TU Delft

This thesis is confidential and cannot be made public until December 31, 2017.

Preface

Photovoltaic solar cells based on $Cu_2ZnSn(S,Se)_4$ (kesterite) compounds are interesting as a potential source of solar energy that is only a few micro-meter thick, consists of earth abundant elements and is low on toxicity, cost and energy payback time. The main contribution of this thesis lies in the experimental investigation of some of the most crucial challenges and opportunities for this family of photovoltaic materials. All experiments were executed in the 'Alternative Thin-Film Photovoltaic' group at imec in Leuven, Belgium, under the European Union's SWInG Horizon 2020 project.

I would like to express my heart-felt gratitude to Prof. dr. Bart Vermang, Dr. Marc Meuris, Dr. Guy Brammertz and Prof. dr. ir. Jozef Poortmans for providing a unique environment of independent research and an invaluable learning experience. Special gratitude is also due to the many members of the thin-film photovoltaic group, III-V team and silicon photovoltaic group at imec for their training and support. I am also grateful to the members of the thesis committee, Prof. dr. ir. Arno Smets, Dr. Olindo Isabella and to the staff and students of the 'Photovoltaic Materials and Devices' group at the Delft University of Technology for their support. The final gratitude is reserved for my family and friends in India and Germany, who helped me reach the Netherlands and set sail on a promising expedition in photovoltaic technologies.

Siddhartha Garud
Delft, July 2017

Cover page: The upcoming site of Energyville in Genk, Belgium, where research on new sources of renewable energy will succeed the old coal mines of the region. *Photo: Rob Stevens/EnergyVille.*

Abstract

In the previous decade, $Cu_2ZnSn(S,Se)_4$ (kesterite) compounds have attracted the interest of several research groups across the world. Their efforts have improved this technology from 5 % power conversion efficiency in 2004 to above 13 % in 2017 (communicated but not published) [1]. This thesis begins with an assessment of the current status of this technology which formed the motivation for the reported experiments.

In particular, the open-circuit voltage (V_{OC}) has been identified as one of the biggest challenges of this technology. To address this issue, a simple, non-vacuum, spin coating technique was developed for the introduction of alkali ions (Li^+, K^+, Rb^+) into a pure selenide $Cu_2ZnSnSe_4$ absorber. The highest V_{OC} achieved with this method was 454 mV, which is approximately 50 mV above the baseline level and on par with the highest known values for $Cu_2ZnSnSe_4$ solar cells [2]. The presence of Rb^+ and Li^+ ions in particular, was observed to reduce recombination in the bulk material and the quantity of shallow defects within the bandgap. Bandgap variations and electrostatic potential fluctuations in conduction and valence bands were investigated as aspects likely affected by alkali ions.

In order to exploit the potential for bandgap engineering of this material, $Cu_2ZnGeSe_4$ based solar cells were developed with experiments for the selection of appropriate substrates, absorber thickness and chemical etching of unwanted compounds. The highest efficiency achieved was 5.9 %, which is close to the state of the art for this material at the time of the writing of this thesis.

Experiments were also conducted to modify the solar cell architecture by introducing a Al_2O_3 passivation layer deposited by atomic layer deposition. A maximum short-circuit current density of 36 mA/cm^2 was achieved but important questions were raised about the dominance of the bulk material in this improvement.

Contents

List of Figures

List of Tables

Nomenclature

A	Solar cell diode ideality factor
AZO	Aluminium doped Zinc Oxide
c-Si	Crystalline silicon
CBD	Chemical Bath Deposition
CBO	Conduction Band Offset
CIGS(e)	$Cu(Ga,In)(S,Se)_2$
CZTS	Cu_2ZnSnS_4
CZTSe	$Cu_2ZnSnSe_4$
CZTSSe	$Cu_2ZnSn(S,Se)_4$
Device	Collection of multiple solar cells
Efficiency (η)	Power conversion efficiency in percentage, under AM1.5G illumination
Eg	Bandgap energy
EQE	External quantum efficiency
FF	Fill factor under AM1.5G illumination
i-ZnO	Intrinsic Zinc Oxide
IQE	Internal quantum efficiency
J-V	Current density and voltage characteristics
J_0	Dark saturation current density
J_{SC}	Short-circuit current density under AM1.5G illumination
Kesterite	$Cu_2Zn(Sn,Ge,Si)(S,Se)_4$
PL	Photoluminescence
PV	Photovoltaic
R_s	Series resistance in solar cell
R_{sh}	Shunt resistance in solar cell
Selenium annealing	Annealing in a selenium atmosphere
SLG	Soda lime glass
STC	Standard Test Conditions
TCO	Transparent Conductive Oxide
$TRPL$	Time-resolved photoluminescence
V_{OC}	Open-circuit voltage under AM1.5G illumination
V_X	’X’ atom vacancy defect
X_Y	Anti-site lattice defect of ’X’ atom in ’Y’ site
XRD	X-ray diffraction

1

Introduction

In 1958, the 'Vanguard 1' satellite was launched into orbit around the earth. It was mankind's fourth satellite and the first one to be powered by photovoltaic cells. This aptly named satellite marked the start of the modern solar age and the ever-growing interest of mankind in tapping the boundless energy of the sun. At the time of this writing, the world faces imminent threats of climate change and also stands at the frontier of a new era in space exploration. At the same time, many parts of the developing world are yet to be connected to a systematic power source. Rapid expansion in photovoltaic systems is predicted from the 242 GWp cumulative installations till 2015 to 400 GWp-600 GWp by 2020 [8–10]. Innovation in photovoltaic technologies can help mankind meet these grand challenges.

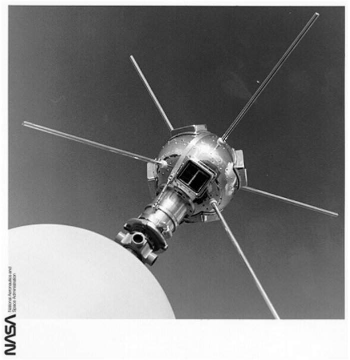

Figure 1.1: An image of the Vanguard 1 satellite with its solar cells in the centre [3].

The motivation of this thesis was to contribute to the development and understanding of solar cells based on the quaternary compounds $Cu_2ZnSnSe_4$ and $Cu_2ZnGeSe_4$. Such materials consist of earth-abundant elements and have the potential to be photovoltaic technologies on the Terawatt scale of global power consumption, with low cost and energy pay-back time. They have a direct bandgap which is also tunable based on the quantity of sulphur and selenium as anions and tin, germanium and silicon as cations. Such characteristics are typical advantages of thin-film solar cell materials. The work presented in this thesis was part of the European Union's SWInG Horizon 2020 project, the ultimate goal of which, is to build a high bandgap thin-film material for tandem solar cells. These cells, with one part each for absorbing the short and long wavelengths of incident radiation, have the potential to produce efficiencies above 30 % which can not be reached by single junction silicon solar cells.

The next three sections elaborate further on why thin-film solar cells are attractive for research and development.

1.1. The case for thin-film solar cells

Wafer based, crystalline silicon technologies have dominated the commercial PV industry, amounting to 93 % of the total production in 2015 [8]. They power the 1.7 million solar panels in the 'Solar star' installation and the Tesla roof tiles that are scheduled to go into production in 2017. Silicon is also the life-line of the electronics industry and has greatly benefited from transistor research and its economics of scale. Nevertheless, given the predicted expansion of the PV market, it is safe to say that there is a large market for alternative materials and technologies such as CIGS(e), CdTe, kesterites (CZTSSe) and perovskites. Even in competition with silicon, there are a number of areas in which other materials can potentially provide better properties:

1. **Absorption**: Silicon is an indirect bandgap material with a relatively low absorption coefficient. A minimum thickness of 40 µm to 100 µm is required to effectively absorb the light incident on it. Wafer based processing techniques currently restrict the minimum thickness to 180 µm. An even greater material wastage is caused due to the common 'wire-saw' wafer cutting technique in which 50 % of silicon is wasted and has to be recycled. In contrast, common thin-film technologies need only 2 µm for complete absorption of light and are commonly grown/deposited on a substrate in a bottom-up approach.

Thin-film technologies have the potential to be lighter, cheaper and more flexible. This makes them particularly interesting for building integrated PV (BIPV) applications [11].

Due to their crystalline nature, silicon wafers work best under direct incident light which is difficult to track as the sun moves in the sky. Amorphous thin-film technologies have a lesser performance drop under indirect light and can be competitive in producing more energy in a day. Average energy production is often a better performance measure than peak power conversion efficiency when comparing different energy sources.

2. **Production**: Silicon is the second most abundant element in the earth's crust in the form of silica (sand). However, SiO_2 is an extremely stable compound. The extraction of electronic grade silicon via the Siemens process is now highly standardized, but it still remains energy intensive ($> 120\,\mathrm{kWh\,kg^{-1}}$) and expensive [11]. Alternative materials can be easier to produce and have lesser energy payback time. Their production can even be solution based as demonstrated by perovskite, organic and kesterite solar cells.

3. **Bandgap engineering**: William Schokley and Hans-Jaochim Queisser famously calculated that an ideal single junction solar cell intended to absorb the sun's light on the earth's surface should have a bandgap between 1.2 eV-1.34 eV [12]. Silicon has a bandgap at a favourable 1.12 eV. Multi-junction solar cells; however, can theoretically go up to 86.6 % efficiency under concentrated light [13]. Since crystalline silicon cannot offer significantly flexibility in tuning the bandgap, it is not attractive for multi-junction applications. Multi-elemental compounds such as chalcopyrites and kesterites can be tailored to different bandgaps by changing the chemical composition. Kesterite solar cells for example, have been created at bandgaps from 1 eV ($Cu_2ZnSnSe_4$) to 1.5 eV (Cu_2ZnSnS_4). With the incorporation of Ge (Cu_2ZnGeS_4), this bandgap could also be increased to 1.9 eV [2].

1.2. Chalcopyrite solar cells

CIGS(e) solar cells of the chalcopyrite crystal structure have been the champions of thin-film technologies, with record laboratory efficiencies reaching 22.6 % which is greater than the multi-crystalline Si record of 21.9 % [5] and comparable to the mono-crystalline Si record of 25.6 % [8, 14, 15]. CIGS(e) solar cells have also exhibited high volume production (1.1 GWp in 2015) and roll-to-roll manufacturing. However, production will required further expansion to match the annual PV production (57 GWp in 2015) and the annual global power consumption on the order of 15 TW [1, 8].

One of the major drawbacks of CIGS(e) technology is the use of indium, which has an estimated abundance of 0.049 ppm in the earth's crust, making it rarer than even silver [16]. Its demand has been rapidly increasing due to its widespread use in touchscreen displays and liquid crystal displays. Gallium also carries a risk of increasing costs. The economics of constituent elements have raised concerns about the scalability of CIGS(e) to the terawattt levels needed for global energy consumption. Within the European Union, both indium and gallium are part of a list of 20 critical raw materials (CRM) due to their contribution to the EU GDP and their supply risk. China currently produces 58 % and 69 % of the world's indium and gallium, respectively [17].

1.3. Kesterite solar cells

Kesterite ($Cu_2ZnSn(S,Se)_4$) solar cells seek to solve the aforementioned challenges of CIGS(e) technology by using earth abundant materials such as copper, zinc, tin, selenium and sulphur. This material was first noted for it's material properties in 1988 and the first solar device was created in 1996 with 0.7 % efficiency. There was limited research till 2004 when a 5 % efficiency cell was demonstrated [1]. A record efficiency of 12.6 % was demonstrated by the IBM T.J.Watson Research Centre in 2014 [18]. Another record efficiency of 13.9 % was announced in 2017 by the Daegu Gyeongbuk Institute of Science and Technology in South Korea. The publication of this result is still awaited at the time of the writing of this thesis.

One of the most impressive aspect of kesterite technology is the ease and variety of production techniques. Most of them require a thin-film deposition step followed by a moderate temperature anneal (500 °C-600 °C) in a gaseous environment. Briefly stated, the various deposition techniques are [19]:

1. **Vacuum based methods**: Sequential or parallel sputtering and evaporation
2. **Nonvacuum based methods**: Spin coating, pyrolytic and non-pyrolytic spray, electrochemical deposition and nanoparticles via hot injection or doctor-blade

1.4. Kesterite cell architecture

After the formation of the kesterite material and subsequent layers, the final cell architecture is as shown in Figure 1.2. Chapter 2 explains the details of fabrication steps followed in this work. The architecture is based on the popular CIGS(e) cell architecture due to the similarities in the absorber materials. Molybdenum is used as a back contact due to its high work function, adhesion properties and reflectivity. Since the kesterite material is p-type, a CdS buffer layer is used to form the pn junction. Intrinsic ZnO and Al-doped ZnO form the transparent conductive oxide layer (TCO) on the top. For better electron collection, a front grid of Ni-doped Al is also deposited on top. Finally, indium is soldered to form a robust electrical connection between measuring probes and the Molybdenum back contact. Each solar cell used in this work measures 0.5 cm^2 in area. On a device of 5 cm × 5 cm, 30 such cells are created and characterized to statistically obtain data for any experiment. One such device is shown in Figure 1.3.

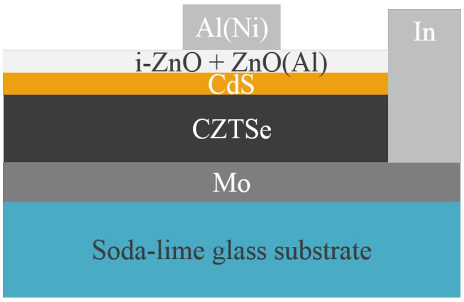

Figure 1.2: Solar cell architecture utilized in this work.

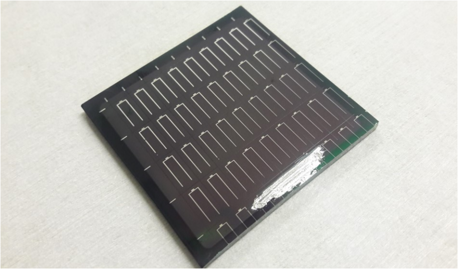

Figure 1.3: Optical image of a 5 cm × 5 cm device with 32 cells of 0.5 cm^2 area each.

1.5. Motivation and outline of the thesis

Two essential elements for the invention of any novel photovoltaic cell are: a semiconductor material with a suitable band structure and a cell architecture that is efficient in carrier collection. Accordingly, the work in this thesis began with experiments to understand and improve the energy band structure. Thereafter, innovative improvements on cell architecture were also attempted.

As a starting point, **chapter 2** details the crystalline structure, band structure and prior art in solar cell development for this technology. By doing so, it gives more details on the motivation for the experiments in this work. It is followed by **chapter 3** which explains the fabrication and characterization techniques utilized.

The focus of **chapter 4** is on the reduction of shallow defects in the band structure which create sub-bandgap states and lower the maximum achievable open-circuit voltage. This was attempted via the addition of alkali ions of Na^+, Li^+, K^+ and Rb^+ to the $Cu_2ZnSnSe_4$ absorber. Extensive studies have not been attempted yet with Li, K and Rb, which makes the work in this thesis particularly useful to the scientific community. It was presented in a poster format at the European Materials Research Society's conference in May 2017 and is under review for publication, as of the time of this writing. The highest open-circuit voltage achieved was 454 mV with Li-doping, which is on par with the record highest V_{OC} for pure selenide $Cu_2ZnSnSe_4$.

Chapter 5 details experiments to create a high bandgap solar cell as well as avoid deep defects that can be created by Sn states. This was done by the substitution of tin with germanium to form $Cu_2ZnGeSe_4$. These experiments lead to the selection of a suitable substrate for future work in this team and to an increased understanding of the bulk material, chemical cleaning steps and surface passivation. The highest achieved cell efficiency was 5.9 %, which is close to the state of the art in this technology.

Chapter 6 reports experiments with atomic layer deposition (ALD) of Al_2O_3 between the $Cu_2ZnSnSe_4$ and CdS layers as visible in Figure 1.2. The reduction of recombination at the surface can lead to an improved carrier collection. Highly conformal deposition techniques such as ALD could also passivate pin holes in some cases and reduce recombination losses in the bulk [20]. The highest achieved J_{SC} through this method was 36 mA/cm^2.

Finally, the finding of this thesis are summarized in **chapter 7** and recommendations are made for the future research directions.

2

Theory and Prior art

2.1. Crystalline structure

In order to understand the chemical origin of the experimentally observed semiconductor physics in CZTSSe materials, it is important to first introduce its crystalline structure. The most energetically favourable structure of CZTS(e) has been accepted to be the kesterite structure shown in Figure 2.1. This structure derives its name from the naturally occurring mineral Cu_2(Zn,Fe)SnS_4. It consist of two alternating cationic planes; one with Sn and Cu and the other with Cu and Zn. These cationic planes are seperated by anionic planes made of Se and/or S. The oxidation states of the constituent elements are: Cu^{+}, Zn^{+2}, Zn^{+4} and S/Se^{-2}. This lattice can have a variety of point defects, namely, anti-site, vacancy or interstitial defects. Their probability of occurrence depends on their enthalpy of formation. The p-type nature of CZTS(e) is attributed primarily to Cu vacancies and in some studies, to Cu occupying Zn sites. Other defects can create deep and shallow states with the desired bandgap. Figure 2.5 created from density functional theory (DFT) simulations by Chen et al. shows all probable defects and their estimated levels in the bandgap for $Cu_2ZnSnSe_4$ [2]. One method to experimentally detect the presence of these defects in a given material is temperature dependent admittance spectroscopy.

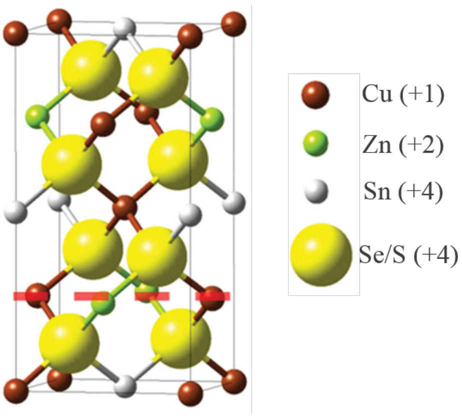

Figure 2.1: Kesterite structure with a dashed line marking one of the two Cu/Zn planes [2].

2.2. Current status

The published record efficiency in CZTSSe solar cells currently stands at 12.6 % as demonstrated by W. Wang et al. in 2014 [18]. On one hand, this efficiency is not unusual for a technology that achieved 5 % in 2004. Table 2.1 highlights that other thin-film technologies have undergone a similar progression, albeit in a different era on scientific research. On the other hand, since this record was set in 2014, a temporary stagnation seems to have occurred in cell improvement. This inevitably raises questions about the ultimate potential of this material and the scientific efforts required to reach it.

Technology	Efficiency, year	Efficiency, year
CdTe	6 %, 1972	12.8 %, 1984
CIGS(e)	5.7 %, 1977	12.2 %, 1988
a-Si	4.8 %, 1978	11 %, 1992
CZTSSe	4 %, 2004	12.6 %, 2014

Table 2.1: Various thin-film technologies have undergone similar progress in a span of ten years [7].

2.2.1. Open-circuit voltage deficit

Several groups investigating the aforementioned stagnation in the development of higher efficiencies have converged towards the open-circuit voltage (V_{OC}) deficit as the main hurdle, defined as:

$$V_{\text{OC-deficit}} = \frac{E_{\text{g}}}{e} - V_{\text{OC}} \tag{2.1}$$

where E_g is the bandgap of the material and e is the elementary charge.

This point is illustrated by Table 2.2 which compares the electrical parameters dictated by the shockley-quiesser (SQ) limit to the record 12.6 % efficiency CZTSSe cell and the pure selenide based 9.7 % efficiency CZTSe cell developed by Brammertz et al. The latter is an in-house record at imec for a (1 cm^2) cell and among the highest pure selenide cell efficiencies [2]. On close inspection of the J_{SC}, V_{OC} and *FF* values, it can be said that while good carrier collection properties have been demonstrated, higher energy conversion efficiencies require higher V_{OC} and fill factor (*FF*).

Technology	Source	Bandgap [eV]	η[%]	J_{SC}[mA/cm^2]	V_{OC}[mV]	*FF*[%]	Reference
CZTSSe	IBM	1.12	12.6	35.2	513	69.8	[18]
CZTSe	imec	1	9.7	38.9	408	61.4	[21]
CZTSSe	SQ limit	1.13	31	43.4	820	87.1	[19]

Table 2.2: A comparison of electrical parameters in record cells with the SQ limit highlights the need for improvement in V_{OC} and *FF*

The causes of a large V_{OC} deficit can be deep defects or shallow defects. These are discussed in detail in the next two sections. The problem of V_{OC} deficit has been the focus of the work discussed in chapter 4 for pure selenide CZTSe devices. In such devices, the front interface with the CdS buffer layer and the back interface with the Mo layer are not expected to limit the V_{OC}. The CZTSe-CdS interface has been the topic of several scientific discussions in recent years and is now generally agreed to have a desirable 'spike-like' conduction band offset in the case of the pure selenide compound CZTSe [2]. The V_{OC} deficit then, may arise primarily from the bulk material.

2.3. Shallow defects

'Shallow' energy states just below the conduction band or above the valence band can lead to an extension of states that electrons can occupy within the bandgap of a material. This leads to a reduction in the fermi-level splitting, an increase in non-radiative recombination and ultimately, a lowering of the upper limit on the achievable V_{OC}. Evidence for such sub-bandgap energy states is shown in the example $Cu_2ZnSnSe_4$ solar cell of Figure 2.2. The peak of the photoluminesence response corresponds to the dominant radiative recombination. It is below the expected bandgap of the material as expected from the EQE of the solar cell. Detailed analyses of such observations were the focus of the study in chapter 4.

The leading theorized cases of sub-bandgap absorption or 'band tailing' as evidenced in Figure 2.2 are:

1. **Spatial variations in the bandgap**: As illustrated in Figure 2.3, they lead to a lower than expected 'average' bandgap. They may arise from spatially varying S/Se content (in case of CZTSSe but not CZTSe) or cation disorder in the lattice.
2. **Electrostatic potential fluctuations**: These are parallel shifts in conduction and valence band energies that do not change the bandgap at any position but can lead to non-local recombination. Figure 2.4 illustrates how such fluctuations can create paths for non-local transitions with energy less than the bandgap. They are attributed to compensating donors and acceptors.

Both phenomena may stem from anti-site point defects such as the acceptor type Cu_{Zn} and donor type Zn_{Cu} since Cu^+ and Zn^{+2} have similar ionic radii and are able to swap atomic sites. The neutral defect pair [$Zn_{Cu}{}^+$ + $Cu_{Zn}{}^-$] has the lowest enthalpy of formation among all defect complexes according to density functional theory calculations [4]. Their effects are further exacerbated by the relatively low dielectric constant of kesterite materials (estimated as 8.5 for CZTSe and 6.7 for CZTS) [21, 22]. Neutron scattering, synchrotron X-ray studies, Raman spectroscopy, nuclear magnetic resonance and scanning transmission electron microscopy of the two Cu/Zn planes shown in Figure 2.1 have created valuable evidence of such a so-called 'Cu/Zn disorder' in the lattice. Transition temperatures around 200 °C and 260 °C for CZTSe and CZTS respectively, have been identified [23–25].

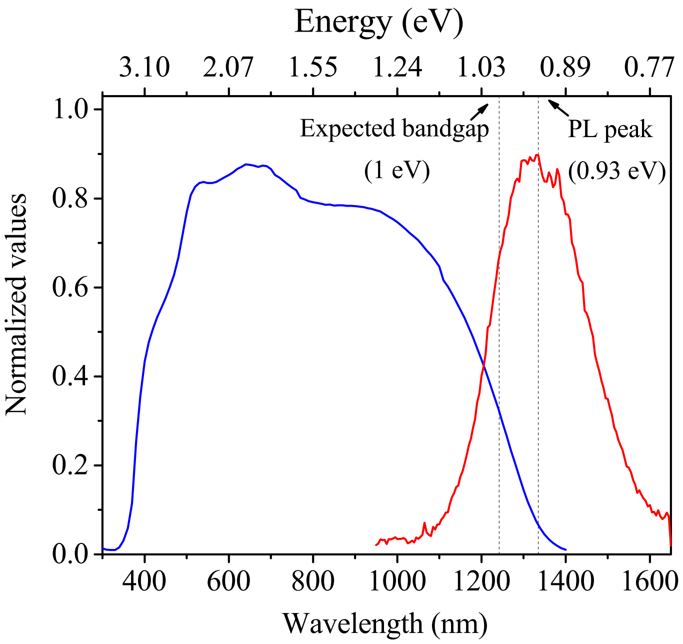

Figure 2.2: A red-shift in the photoluminescence peak away from the bandgap expected from *EQE* shows evidence of shallow states below the bandgap.

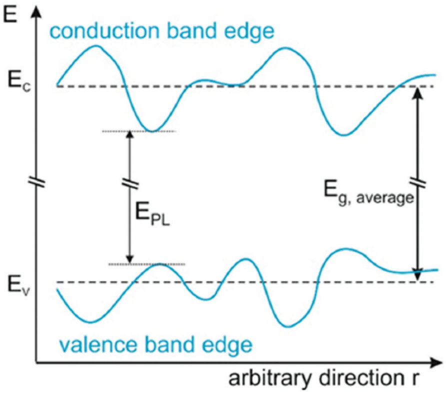

Figure 2.3: Bandgap fluctuations in the conduction and valence bands leading to a lower average bandgap [2].

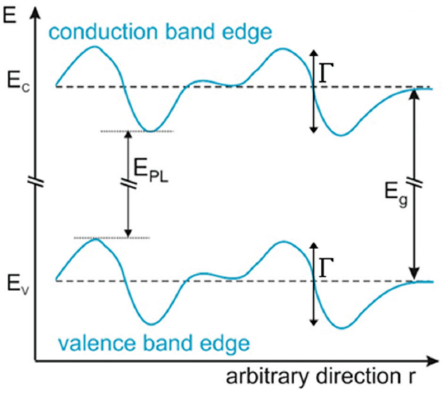

Figure 2.4: Electrostatic potential fluctuations in the conduction and valence band shown at a constant direct bandgap [2].

It is also important to note that the p-type doping in kesterite solar cells is often attributed to shallow (50 meV) copper vacancies (V_{Cu}) but sometimes also to the deeper (110 meV) Cu_{Zn} defect. Such point defects are therefore, an inherent part of the material and may decide the ultimate potential of this technology.

It is essential to note that this issue does not exist in CIGS(e) cells due to the different ionic radii and chemical nature of Cu^+ and In^{+3}/Ga^{+3}. Band tailing has also been observed to be consistently lower in CIGS(e) cells although it does exist to some degree [22].

2.4. Deep defects

Defects close to the middle of the bandgap of a material can greatly increase non-radiative recombination and severely hinder the performance of a solar cell. Referring to Figure 2.5 again, we can see that Sn_{Cu} and Sn_{Zn} are both likely deep donor type defects. Therefore, a Sn-poor material might be desirable but a lack of sufficient Sn can also create deep acceptor type V_{Sn} vacancy. Larramona et al. have shown that tuning of Sn content in CZTSSe can help achieve efficiencies upto 10.8 % [26]. Extensive analysis in admittance spectroscopy led them to the conclusion that they were able to reduce deep defects in the material possibly arising from V_{Sn} and/or Cu_{Sn} defects. The volatility of Sn and its compounds such as $SnSe_2$ during the annealing step(s) can create such deficiencies and additionally, reproducibility issues.

Edgardo et al. have shown that incorporation of Ge in small quantities can promote large grain growth and also possibly reduce the formation of deep defects associated with Sn^{+2}. A top cell efficiency of 10.6 % was achieved on a pure selenide cell (CZTSe + Ge) [27]. Other research groups in the European Union's SWInG project, have begun to entirely replace Sn with Ge in order to create a more stable $Cu_2ZnGe(S,Se)_4$ material. An important aim of this project are tandem solar cell applications since the incorporation of germanium and sulphur can increase the bandgap of CZGSSe from 1.4 eV (pure Selenium) to 1.6 eV (desired high bandgap) and 1.9 eV (pure sulphur). Chapter 3 shows developments made in this work under this project.

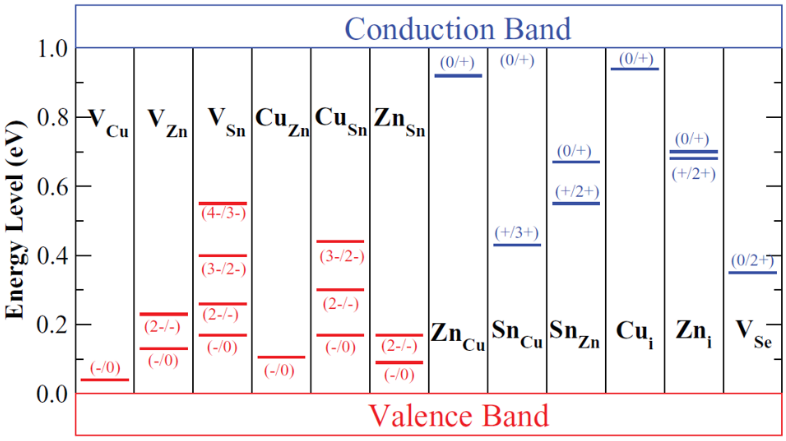

Figure 2.5: Sub-bandgap defects shown according to their ionization levels with red coloring for acceptor levels and blue for donor levels. Reproduced with permission [4].

2.5. Secondary phases

$Cu_2ZnSnSe_4$ is a quartenary compound with the elements possessing the oxidation states Cu^+, Sn^{+2}, Zn^{+2}, Se^{-2}. The formation of such a complex compound is not without difficulties. In competition with the enthalpy of formation of $Cu_2ZnSnSe_4$, certain binary and ternary compounds are also stable and can be formed easily. These include ZnSe, SnSe, $SnSe_2$, CuSe, Cu_2Se and Cu_2SnSe_3. In large quantities, ZnSe can create high series resistance and cause adhesion issues. However, the other listed phases are considered more harmful since their low bandgap can severely reduce shunt resistance in a cell. This is one of the reasons why several teams have observed that a Cu-poor and Zn-rich composition is important for cell performance [1, 2, 28]. In order to remove at least the secondary phases and oxides accumulated at the absorber-air interface, several teams resort to an etch step with KCN, HCl, bromine-methanol solution, $(NH_4)_2S_x$ or other chemicals [29].

3

Experimental procedure

3.1. Fabrication steps

In the work presented in this thesis, kesterite compounds were made through a so-called 'sequential process'. All the steps are illustrated in Figure 3.1 and are described in the following sections.

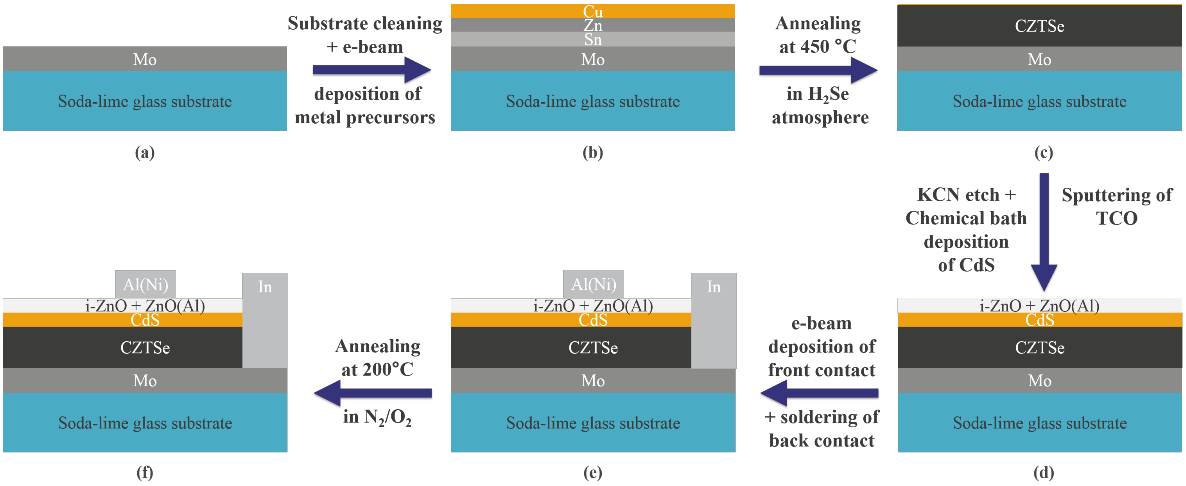

Figure 3.1: Schematic representation of the general fabrication steps followed in this work.

3.1.1. Cutting and cleaning

The standard substrate used was a 3 mm soda lime glass with 400 nm of molybdenum sputtered on one side. It is first cut into smaller pieces of 5 cm × 5 cm or a half size of 2.5 cm × 5 cm. An industrial diamond tip is used for cutting the glass.

The molybdenum surface is cleaned by dipping the substrate in 30 wt% NH_4OH for 6 minutes. This removes any organic matter or oxides such as MoO_3 present on the surface. The substrates are then dipped in water and isopropyl alcohol for 6 minutes each and then dried with an N_2 gun.

3.1.2. Electron-beam deposition of metal precursors

The cells are fabricated in a 'substrate' configuration meaning that soda lime glass is the bottom-most layer. This process is called 'sequential' because metal precursors layers are sequentially evaporated onto the Mo surface. The stack order shown in Figure 3.1(a) was finalized after previous work in this team. The evaporation of the metals was done with an electron beam in a Pfeiffer vacuum chamber at a pressure of 10^{-6} mbar. The evaporation chamber can hold up to four ingots and hence, no break in the vacuum was required for any deposition. A high voltage of 10 kV is applied to a filament to generate an electron beam. A magnetic field is used to direct the electron beam onto an ingot of the target material. The beam is swept over a small area in order to heat the target uniformly. A schematic of this apparatus is shown in Figure 3.2. The deposition rate used was 6 Å per second, as measured with a quartz crystal. Substrates were rotated continuously during the deposition for homogeneity.

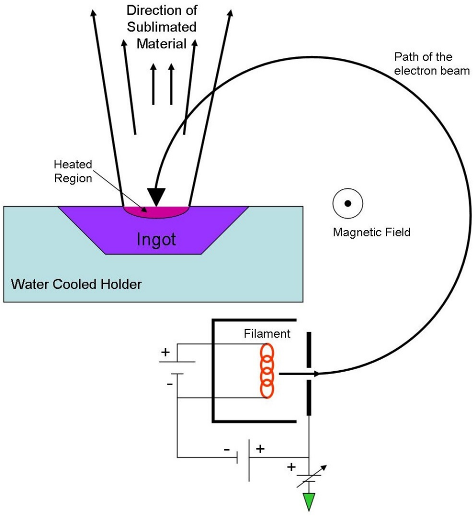

Figure 3.2: Schematic representation of the electron beam deposition of metal precursors [5].

Trials were conducted to select an optimal thicknesses, with the work by Samaneh et al. as a starting point [30]. Ultimately, 310 nm of tin, 165 nm of zinc and 160 nm of copper were used to make $Cu_2ZnSnSe_4$. In chapter 4, some more steps are described that were taken to spin-coat alkali salts on top of the copper surface created after this step. Shortly before the experiments of chapter 5 on $Cu_2ZnGeSe_4$ material, another optimized stack was created with 180 nm of germanium, 125 nm of zinc and 170 nm of copper.

3.1.3. Annealing in a Selenium atmosphere

Substrates were then heated in an annealing step of 15 min at 450 °C with 200 sccm flow of 10 % H_2Se gas diluted in N_2. A graph of temperature versus time for this step is shown in Figure 3.3. Halogen lamps are the source of heat and a ramp of 1 °C/s is used to raise the temperature to 450 °C. A graphite receptacle is used to hold the substrates. A thermocouple is inserted into this receptacle to measure the temperature of the chamber. The ramp and 15 minute annealing steps cause chemical reactions between the metals and selenium to create $Cu_2ZnSnSe_4$ (or $Cu_2ZnGeSe_4$) and other compounds with a competitive enthalpy of formation. At this temperature, H_2Se breaks down into hydrogen and selenium and the hydrogen atoms do not seem to have any significant effect on the absorber. A similar supply of H_2S is also available for reactions with sulphur.

3.1.4. KCN etch

Based on previous studies by Buffiere et al. substrates are dipped in 5 wt% KCN for 2 minutes in order to remove unwanted binary compounds accumulating at the surface during the selenium atmosphere annealing [31]. This is a step the author did not perform since only a fixed number of trained personnel are allowed to use KCN. It is used in the results of chapter 4 and chapter 6 based on $Cu_2ZnSnSe_4$ absorbers. It was initially not used on the $Cu_2ZnGeSe_4$ absorbers of chapter 5 due to adhesion issues but was later studied again for its effect on this new material.

3.1.5. Atomic layer deposition (ALD)

In the work presented in chapter 6, atomic layer deposition was used at this stage to form a passivation layer of Al_2O_3 on top of the absorber layer. ALD generally consists of two (or more) exposures to precursors with each one causing 'half' of a reaction. These exposures are separated by a purge step. Each exposure is self-limiting, meaning that one atomic layer of a certain precursors is deposited on top of the other precursor and no further deposition takes place. An illustration of the cycles involved in the experiments of chapter 6 is shown in Figure 3.4. The nature of self-limitation separates ALD from a chemical vapour deposition which otherwise follows similar chemical reactions to deposit on a target surface. Therefore, ALD requires special precursors and operates in a small temperature window. The physical and chemical effects outside

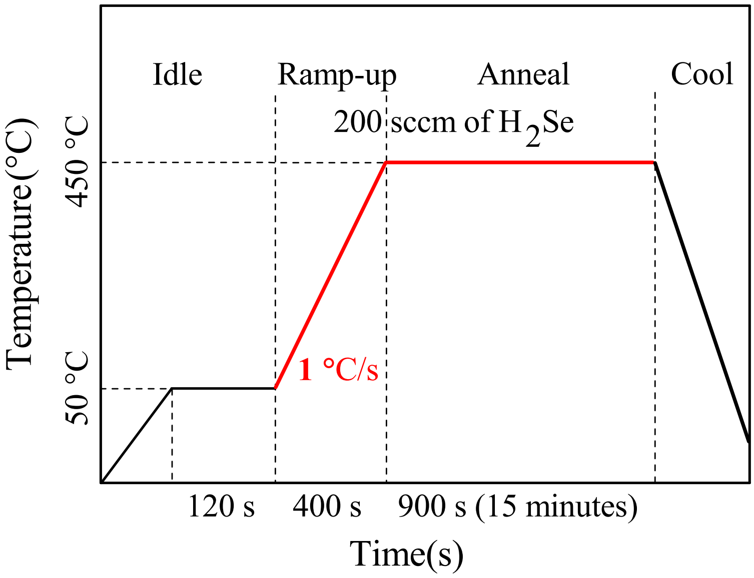

Figure 3.3: A graph of temperature versus time for the main annealing step which causes a chemical reaction between the metal precursors and selenium (or sulphur when required).

this window are shown in Figure 3.5.

In these experiments, trimethylaluminum and water were used as precursors for the self-limiting reaction at 150 °C and 0.5 mbar. A pulse duration of 16 µs for trimethylaluminum and 30 µs for water were used. The estimated growth rate is 0.11 nm/cycle.

3.1.6. Chemical bath deposition of CdS

A standard chemical bath deposition of CdS is then performed to obtain approximately 50 nm of the buffer/n-type layer (Figure 3.1(d)). This is also a step not performed by the author due to the toxicity of cadmium. CdS was used because all the absorbers in the reported experiments are p-type in nature.

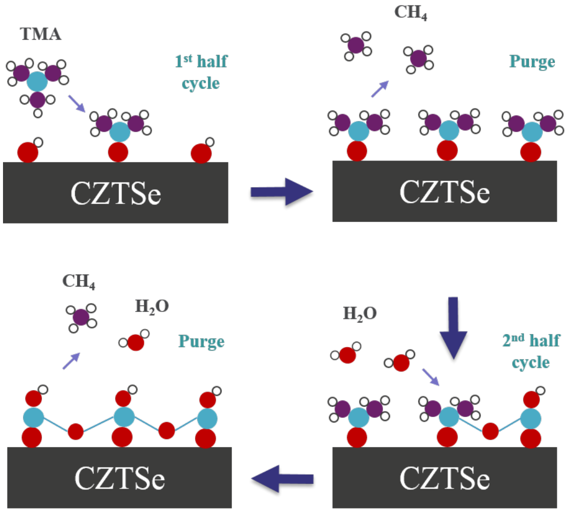

Figure 3.4: Illustration of the various cycles and surface reactions involved in an atomic layer deposition of Al_2O_3.

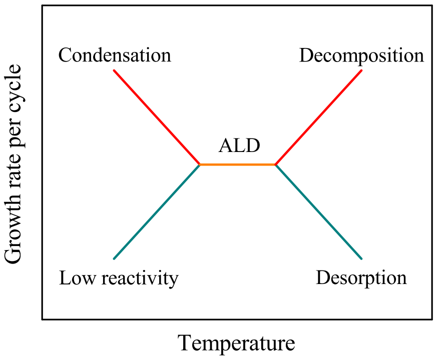

Figure 3.5: Illustration of the temperature window in which a chemical reaction is self-limiting and can be called an atomic layer deposition [6].

3.1.7. Sputtering of transparent conductive oxide (TCO)

For optimal carrier collection, 120 nm of intrinsic ZnO and 250 nm of Al-doped ZnO are sputtered on top of the CdS layer (Figure 3.1(d)). No anti-reflection coating such as MgF_2 was deposited on solar cells developed in this work. Such a layer is expected to give 0.4-1 % absolute improvement in efficiency over the results presented here.

3.1.8. Front and back contacts

In order to create a proper electrical connection between probes and the top TCO layer and bottom Mo contact, front and back contacts are created (Figure 3.1(e)). The front contacts consist of Ni (50 nm)/Al (1 µm)/Ni (50 nm) formed by e-beam deposition and shadow masks, in the same tool as described earlier. Back contacts are made by scribing away all the layers on one side of a substrate and soldering indium onto the molybdenum. Cells of 0.5 cm^2 were isolated by scribing with a mechanised blade.

3.1.9. Annealing of completed cells

Finally, completed devices undergo another annealing step at 200 °C for 1 hour in an N_2 or O_2 atmosphere created in a quartz tube furnace. This step has been experimentally observed to improve the quality of the bulk material by improving open-circuit voltage and fill-factor. The exact mechanism of this improvement is still under study. For the sake of brevity, the characterization data in chapter 4 corresponds to $Cu_2ZnSnSe_4$ cells after this annealing step. In the experiments of chapter 5, this annealing step was not used as it was seen to deteriorate $Cu_2ZnGeSe_4$ cell performance. This step is highlighted again in chapter 6 where it forms an important part of the analyses.

3.2. Characterization techniques

3.2.1. Photoluminescence

Photoluminescence (*PL*) analysis uses a pulsed source of light to excite electrons in a semiconductor material. Luminescence from the radiative recombination of the excited electrons and holes is monitored to identify the dominant wavelengths and intensity of emissions. Such a reading shows the energy difference between the dominant radiative recombination paths, which in an ideal case would be the bandgap of the material. An example is shown in Figure 3.6 where the dominant recombination path has an energy difference of 955 meV corresponding to a wavelength of 1300 nm. If there is more than one such recombination path, then a broader *PL* curve is obtained, sometimes with multiple peaks. Since excited charge carriers are not collected, they all eventually recombine. Therefore, high *PL* intensities indicate that non-radiative recombination is low in a semiconductor, which is desirable.

When the luminescence is measured as a function of time, an indication of the minority charge carrier lifetime can be obtained. An example graph is shown in Figure 3.7 in a semi-log format. Such a reading is fit with 2nd or 3rd order exponential equation. In general, the time constant from the 1st order of fitting corresponds to the fast recombination of excitons and the constant from the 2nd order corresponds to minority charge carrier lifetime. However, this inference is still under debate for kesterite materials. If a 3rd order fitting is also required then the 3rd order constant indicates the presence of charge carrier traps in the bandgap which delay recombination.

In this work, time-resolved photoluminsecene was measured using a Hamamatsu C12132 near-infrared compact fluorescence lifetime measurement tool. The excitation laser has a beam spot of 3 mm diameter and an excitation wavelength of 532 nm. It is a YAG, class 3B laser with a 15 kHz repetition rate and 1 ns pulse length. An average illumination intensity of 1 mW was used. Wherever the photoluminescence response has been compared, care has been taken to ensure that the same optical settings of IRIS and filters were used for each measurement.

3.2.2. Current density and voltage characteristics (J-V)

J-V characteristics of a solar cell essentially show the diode characteristics of a solar cell as modified by a photocurrent generated under illumination. They are not only a measure of the maximum power a solar cell can generate, but also of important electrical parameters such as the current generated by the solar cell in a short-circuit condition, and the voltage generated by it in an open-circuit condition. In this work, J-V characteristics were analyzed using a WACOM solar simulator system with AM1.5G spectrum and a 2401 Keithley source meter. A cell temperature of 25 °C was maintained during measurements. Since the illumination is the main source of heat in this setup, an automatically controlled shutter was used. A one-diode model proposed

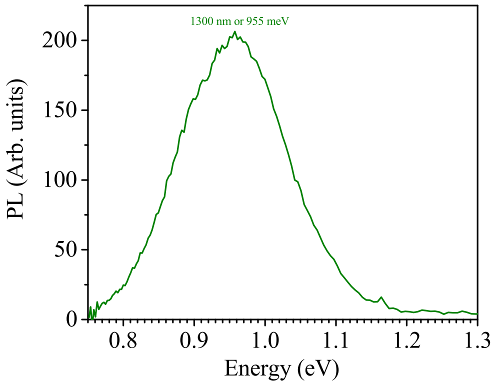

Figure 3.6: Example photoluminescence peak showing the energy level of the dominant radiative recombination path.

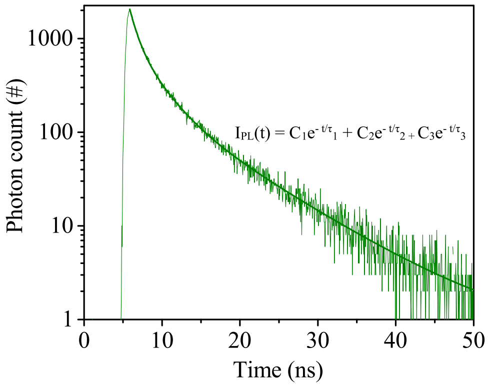

Figure 3.7: Example time-resolved photoluminescence requiring a third order exponential fit.

by Hegedus et al. for thin-film solar cells was applied through a MATLAB code for the electrical characterization of cells [32].

3.2.3. External/Internal quantum efficiency

External quantum efficiency (*EQE*) is the efficiency of a solar cell in converting incident photons into charge carriers collected and transferred to an external circuit. It is measured across the desired wavelength range of incident light. If reflection and transmission losses at various wavelengths are also measured, then an internal quantum efficiency (*IQE*) can be calculated. It is the efficiency of the solar in generating electrons from absorbed photons. The measurement tool used in this work was a home-built system with chopped light from a xenon lamp and a grating monochromator in a dual-beam setup.

3.2.4. Capacitance-voltage (CV)

The solar cells fabricated in this work are based on a p-n junction architecture. Therefore, a measure of capacitance of the solar cell over a range of applied voltages can be used to obtain estimates of the depletion region width and majority carrier concentration at the edge of the depletion region. In this work, uniform doping and a one-sided, abrupt junction was assumed for simplicity. The CV measurements were made on an Agilent 4980A LCR-meter with a frequency range of 1 kHz to 1 MHz.

3.2.5. X-ray diffraction (XRD)

X-ray diffraction measurements of the thin-film kesterite material were used to detect crystalline phases present in the absorber such as $Cu_2ZnSnSe_4$ (kesterite or stannite), SnSe, $SnSe_2$ and Cu_xSe. ZnSe produces the same diffraction peaks as $Cu_2ZnSnSe_4$ kesterite and is thus, difficult to detect via this method. A complimentary technique such as Raman spectroscopy can be used instead. A similar analysis was done to detect crystalline phases present in the efforts to create $Cu_2ZnGeSe_4$ absorber layers. ZnSe and $Cu_2ZnGeSe_4$ do not have overlapping diffraction peaks and can be separately detected. In this work, XRD measurements were executed on a PANalytical X'Pert Pro MRD X-ray diffractometer in the conventional Bragg-Brentano $2\theta - \omega$ configuration using a copper Kα (1.5411 Å) radiation as incident beam.

4

Addition of Alkali metals

The treatment of chalcopyrite (CIGS(e)) solar cells with potassium (K-PDT) has been a major breakthrough in achieving efficiencies above 20 %. Thus, sodium, potassium and other alkali elements are of great interest for kesterite solar cells too, due to the structural similarity with chalcopyrite. Many studies show that sodium has a positive effect on kesterite grain size, non-radiative recombination and hole concentration. Sodium is also known to passivate grain boundaries [33]. Based on similar work on CIGS(e) material, it is theorized that sodium may create $\mathrm{Na_{Cu}}$ defects which inhibit the formation of $\mathrm{Zn_{Cu}}$ defects, and/or form $\mathrm{Na_{Zn}}$ defects which increase hole concentration [34]. Theoretical calculations have shown that these effects can also be achieved by other alkali ions as $\mathrm{K_{Cu}}$ and $\mathrm{Li_{Cu}}$ are also favourable substitution defects [35, 36]. This work reports on the improvement of open-circuit voltage $\mathrm{V_{OC}}$ via the addition of Li, K and Rb.

4.1. Spin-coating technique

A simple, non-vacuum spin-coating process was used to introduce alkali ions in the absorber. Following the e-beam deposition described in chapter 3, the top surface (copper), was cleaned with $\mathrm{NH_4OH}$ solution (30 wt%) to make it more hydrophilic. Three spin coating solutions were made with LiF (99.98 % purity, Sigma-Aldrich), KF (99.99 % purity, American elements) and RbF salts (99.8 % purity, Sigma-Aldrich). Deionized water was used as the solvent due to its desired polar nature for these salts. The solutions were heated to 80 °C to reduce surface tension. After static dispensation, the substrates were spun at 5000 RPM for 1 minute. The solution concentrations shown in this chapter have been obtained after optimization by the author. Higher concentrations could be tried through colloidal solutions or by other methods such as thermal evaporation of the salts. A reference device was included which was subjected to spin coating of only deionized water. All the samples were processed together at each step. Sodium diffusion from the glass substrate is also present in all these samples, including the reference. From previous experiments, it is know that a set of samples processed together show similar electrical characteristics. Furthermore, statistical data has been used to show that the higher open-circuit voltages obtained cannot be achieved from the diffused sodium alone. Such high values for this parameter have not been obtained previously in this research group.

After the spin-coating, the substrates were heated in an annealing step at 450 °C with $\mathrm{H_2Se}$ gas diluted in $\mathrm{N_2}$. This step creates the CZTSe absorber layers in the presence of the spin coated Li/K/Rb fluorides. The remaining steps were as described in chapter 3.

4.2. Electrical performance parameters

On every device, 30 cells were electrically characterized. No anti-reflection coating ($\mathrm{MgF_2}$) was deposited on these cells. Nevertheless, the measured values are also compared with the 9.7 % efficiency CZTSe cell developed by Brammertz et al. which is an in-house record for a 1 $\mathrm{cm^2}$ area and among the highest pure selenide performances [21].

The statistical results for the open-circuit voltage are as shown in the box plots of Figure 4.1. The lines of the box plot demarcate the first and third quartile and the middle line marks the median values. The average and extreme values are marked by a dot and crosses respectively.

It can be seen that there is a clear improvement in most of the Li-doped samples as compared to the reference. Over an average of 30 cells, an improvement of 37 mV was observed. The highest V_{OC} recorded was

454 mV.

Even in the case of Rb-doping, the best and median values are higher than reference although there is some overlap in other cells. The average value is 16 mV above the average value of the reference cells. The K-doped samples performed at par or slightly lower than reference but with significant overlap.

Figure 4.2 shows graphs in the same format for short circuit current density (J_{SC}), fill-factor (FF) and overall efficiency (η). There is a reduction in carrier collection (J_{SC}) in the K-doped and Rb-doped samples. A similar trend is observable in the fill-factor. Hsieh et al, have highlighted that optimization of CdS layer can lead to improved performance with K-doping due to surface states [37].

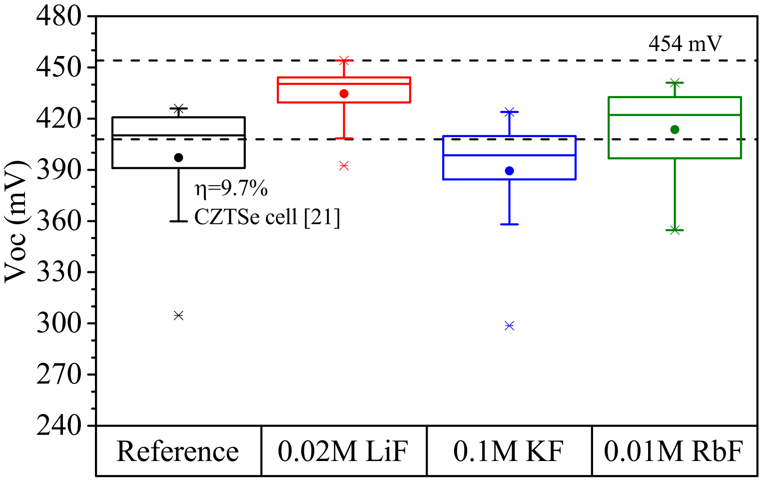

Figure 4.1: Recorded open-circuit voltage (V_{OC}) for 30 cells of 0.5 cm^2, in each case of precursors spin coated with an optimized concentration of fluoride solution.

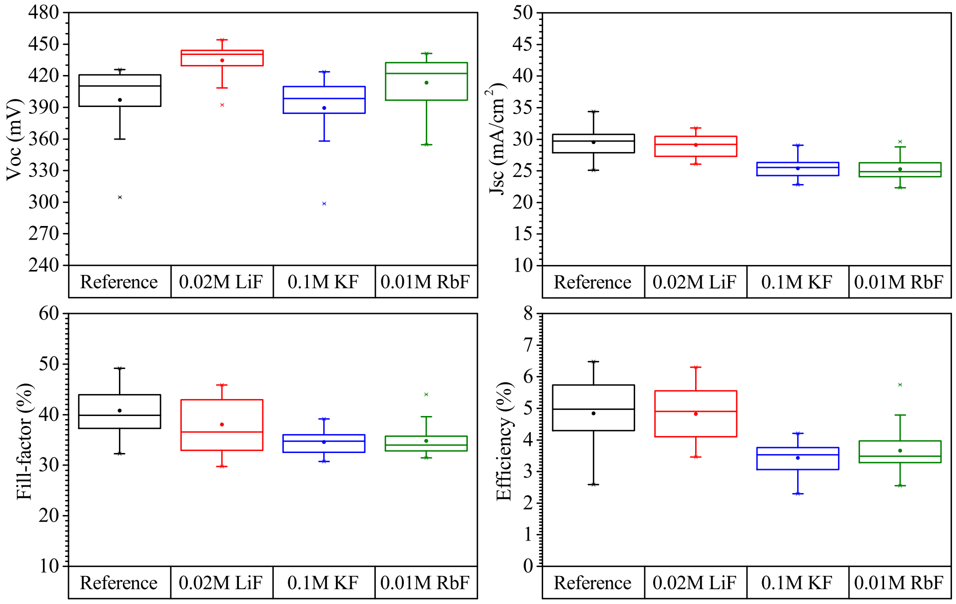

Figure 4.2: Electrical parameters of V_{OC}, J_{SC}, FF and efficiency shown for all cells in this experiment.

The overall efficiencies are affected by these trends in J_{SC} and FF, with the maximum value of 6.5 % in reference and 6.35 % in a Li-doped cell. The relatively poor performance of K-doped cells may be partly attributed to an increased presence of $SnSe_2$ as detected in XRD measurements (not shown here). It can be stated now, that higher *FF* and J_{SC} via optimized selenium atmosphere annealing and CdS deposition are required to achieve efficiency values greater than the referred 9.7 % CZTSe cell [21]. For further analysis of the V_{OC} improvement, the upcoming graphs will focus on the cells with the best V_{OC} in each device (Table 4.1). A V_{OC} of 454 mV was obtained with Li-doping in a cell with 3.9 % efficiency. Nevertheless, Figure 4.2 clearly shows that most cells with Li-doping outperformed the reference cells in V_{OC} while producing nearly the same efficiencies statistically across 30 cells in each device. The highest efficiency produced by a Li-doped cell was 6.3 % with a V_{OC} of 441 mV.

Best cell of device	J_{SC}(mA/cm^2)	V_{OC}(mV)	*FF*(%)	η(%)
Reference	30.8	426.0	48.5	6.4
0.02M LiF	27.1	454.1	31.8	3.9
0.1M KF	25.6	423.3	32.6	3.6
0.01M RbF	29.6	441.1	44	5.7

Table 4.1: Electrical parameters of best V_{OC} cell from each device.

4.3. Reasons for enhanced V_{OC}

A one-diode model developed by Hegedus et al. was used to analyse cell results [32]. In equation 4.1, '*A*' is ideality factor, 'J_0' is dark saturation current density, and 'R_s' and 'R_{shunt}' are lumped series and shunt resistances.

$$J(V) = J_0\left[exp\Big(\frac{e(V - R_\mathrm{s}J)}{AkT}\Big)\Big) - 1\right] + \frac{V - R_\mathrm{s}J}{R_\mathrm{shunt}} - J_\mathrm{SC} \tag{4.1}$$

In an ideal pn junction, J_0 is a function of minority carrier lifetime (τ), mobility/diffusion constant (D) and concentration (n_{p0} for electrons in p-type kesterite)

$$J_0 = \frac{eD_\mathrm{n}n_\mathrm{p0}}{\sqrt{D_\mathrm{n}\tau_\mathrm{n}}} + \frac{eD_\mathrm{p}p_\mathrm{n0}}{\sqrt{D_\mathrm{p}\tau_\mathrm{p}}} \tag{4.2}$$

Thus, three reasons can be considered for an improvement in V_{OC}:

1. Reduction in charge carrier recombination and increase in carrier lifetime
2. Increase in majority charge carrier density
3. Increase in shunt resistance

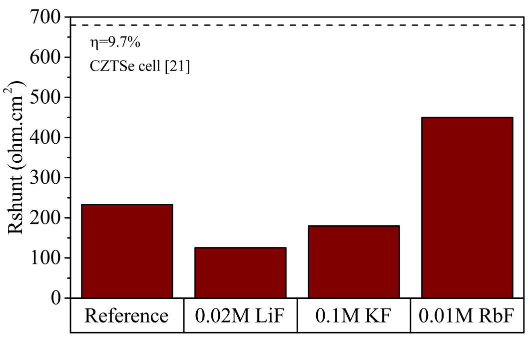

Figure 4.3: Low shunt resistance values were recorded in all cases except Rb-doping, which suggest that they did not contribute significantly to the improvement of V_{OC}.

Shunt resistance values in the best V_{OC} cells of Table 4.1 were calculated to be around 200 Ω cm^2 in all cases except with Rb-doping, in which it was 450 Ω cm^2 (Figure 4.3). Thus, excluding the case of Rb-doping, the R_{shunt} values are too low to explain the improvement of V_{OC}, especially in comparison with the 9.7 %

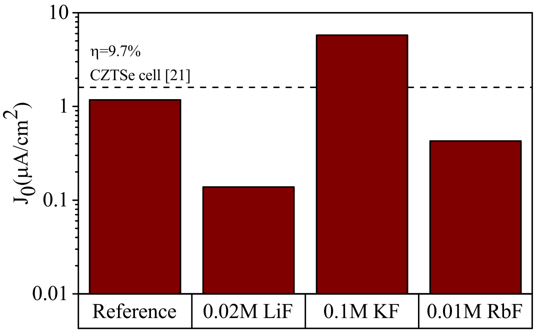

Figure 4.4: Increase in V_{OC} correlates well with the reduction in dark saturation current density (J_0), shown here for the best cells.

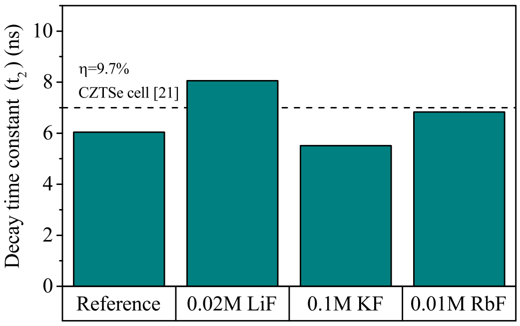

Figure 4.5: Increase in V_{OC} also correlates well with minority charge carrier decay time shown here by a 2nd order exponential fit of the time-resolved photoluminescence (Figure 4.9).

efficiency CZTSe cell which had an R_{shunt} of 680 Ω cm^2. They can, however, help explain the lower fill-factor values (up to 48.5 %) compared to that of the 9.7 % efficiency cell (61.4 %) ([21]).

The trends in the best V_{OC} cells correlate well with the reduction in dark saturation current (Figure 4.4) and increase in minority charge carrier decay time (Figure 4.5). They indicate that reduced recombination in the bulk contributed to improved V_{OC} values. Pure selenide CZTSe cells are particularly useful for this study since the front interface with the CdS buffer layer and back interface with the molybdenum layer are not expected to limit the V_{OC}. After several scientific discussions, the CZTSe-CdS interface is generally expected to have a desirable 'spike-like' conduction band offset [2]. The limitation then, may arise primarily from the bulk material.

A two times higher majority charge carrier density was also observed with Li-doping (Figure 4.6) which would lead to increased quasi-fermi level splitting. In chalcopyrite solar cells, electrostatic potential fluctuations in band edges (explained in the next section) can be screened by sufficiently high density of free charge carriers, leading to higher V_{OC} [2]. A possible reason for this increased hole concentration is the formation of a shallow Li_{Zn} acceptor type defects. They would compete with Cu_{Zn} acceptor defects but if they are shallower, they can create a net increase in hole concentration.

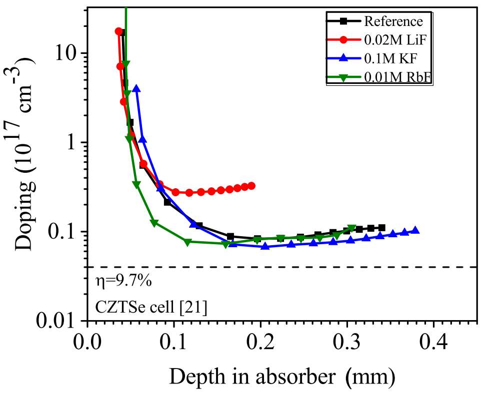

Figure 4.6: An increase in majority charge carrier density with the addition of Li may also contribute to an improved quasi-fermi level splitting and V_{OC}.

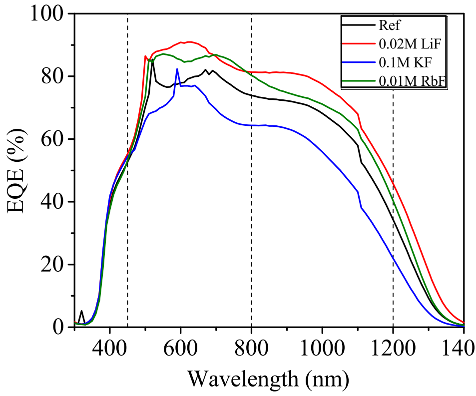

Figure 4.7: A slow decay tail below the expected bandgap (1 eV or 1242 nm) is an indication of absorption of light by energy states below the bandgap. Lines are shown as a guide to the eye.

4.4. Presence of band tailing

The large V_{OC} deficit observed in kesterite solar cells has been attributed at least in part to the presence of sub-bandgap states or 'band tailing' [2, 22, 38]. In this section, we investigate the presence of these shallow states from photoluminescence (*PL*) and internal quantum efficiency (*IQE*). The bandgap of extended states in a semiconductor can be determined by methods such as Tauc's plot, photo-reflectance, electro-reflectance and ellipsometry. However, since most groups working on kesterite material deposit thin-films on a glass + molybdenum susbtrate, alternative analyses with photoluminescence and internal quantum efficiency have been utilized. The molybdenum back contact acts as a back reflector and does not allow any transmission of light through the substrate. *IQE* has been used to obtain a spectrum proportional to the absorption spectrum since (1-*IQE*) is a measure of the transmission of the thin-film absorber [38]. The window layers have negligible absorption near the bandgap energy range of the absorber.

In the presence of band tailing, the inflection point of the *IQE* spectrum in the low energy slope has been proposed as an indicator of the bandgap of extended states [18, 22, 39]. The bandgaps of the best V_{OC} cells obtained through this method were found to be the same in the reference, with Li-doping and Rb-doping (Table 4.2). This is an important result because V_{OC} in kesterite solar cells is known to scale with the bandgap due to lattice order/disorder, without actually affecting the V_{OC} deficit [2, 40].

Figure 4.7 shows the *EQE* of the investigated cells across a broad wavelength range. A slow decay tail is observable below 1242 nm wavelength corresponding to the expected bandgap of 1 eV. This is also an indication of absorption of light by energy states below the bandgap. In an ideal semiconductor, the *PL* peak is obtained at ($E_g + kT/2$) where T is the temperature and k is the Boltzmann's constant. However, in the case of CZTS(e) and CIGS(e), it is observed to be at energies lower than the bandgap energy as already discussed in chapter 2. This indicates the presence of sub-bandgap states from which charge carriers radiatively recombine. Thus, the position of the *PL* peak is an indication of the maximum achievable V_{OC} in a device that is limited by the bulk.

With alkali doping, an increase in radiative recombination, as well as a blue shift in the photoluminescence peak was observed in the room temperature *PL* (Figure 4.8). A maximum shift of 27 meV was observed with K-doping and a shift of 21 meV with Rb-doping as compared to the reference.

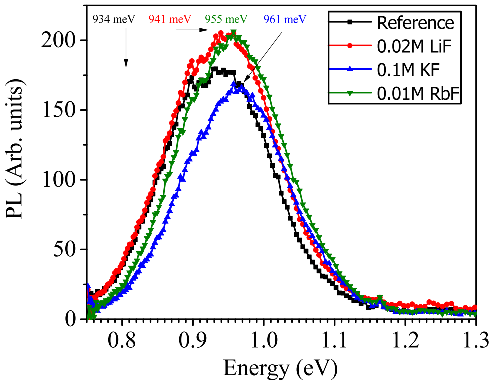

Figure 4.8: Addition of alkali shows increased radiative recombination and blue-shift in room temperature photoluminescence peak which hints towards a reduction in band tailing.

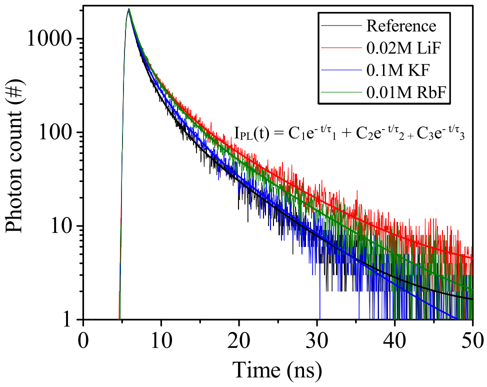

Figure 4.9: Time-resolved photoluminescence shows long decay tails requiring a 3rd order exponential fit.

A reduction in the difference between the bandgap energy obtained from *IQE* and the *PL* peak energy, indicates the reduction of tail states (Table 4.2). The full width half maximum (FWHM) of the *PL* curves did not change noticeably with alkali doping. It is also interesting to note that the K-doped cell showed a slightly higher bandgap in the *IQE*.

Sample	*PL* peak position (eV)	Bandgap from *IQE* (eV)	(Bandgap - *PL* peak) (meV)	FWHM of *PL* (eV)
Reference	0.934	0.992	58	0.177
0.02M LiF	0.941	0.992	51	0.178
0.1M KF	0.961	1.03	69	0.174
0.01M RbF	0.955	0.992	37	0.178

Table 4.2: Evidence of band tailing in *PL* (Figure 4.8) and *IQE*.

Sub-bandgap states may arise from bandgap fluctuations and/or electrostatic potential fluctuations created by compensating defects [2, 22]. Further evidence of the latter was seen in the time-resolved photoluminescence (*TRPL*) (Figure 4.9). The long decay tail required a 3rd order exponential fitting for a chi-factor (error factor) < 1.5. This hints at the presence of traps for charge carriers which delay their recombination. Low temperature *TRPL* measurements of previous devices fabricated with similar process steps have also indicated decay times on the order of µs at 80 K. A similar observation was also made by Gokmen et al. [22]. Electrostatic potential fluctuations lead to spatial separation of charges while bandgap variations do not. Some amount of charges may be able to tunnel to recombine, but a majority of them would be separated by larger distances and would not have the thermal energy to readily recombine at low temperatures.

4.5. Analysis of band tailing

In order to quantify the presence of electrostatic potential fluctuations and bandgap variations, the methods highlighted by Gokmen et al. were used [22].

IQE based on absorption coefficient (α), depletion region width (W) and effective diffusion length (L_{eff}) is: [41]

$$IQE = 1 - \frac{exp(-\alpha W)}{\alpha L_{\mathrm{eff}} + 1} \tag{4.3}$$

Thus, absorption coefficient in the sub-bandgap region (*IQE* < 0.3) in a 1st order approximation of the logarithmic series is:

$$\alpha \propto -ln(1 - IQE) \tag{4.4}$$

The amplitude of purely electrostatic potential fluctuations (γ_{opt}) due to a random distribution of charged defects ($\mathrm{N_t}$) can be modeled on the absorption coefficient (α) [22] as:

$$\alpha \propto exp\left(-\frac{2}{5\sqrt{\pi}}\left(\frac{E_{\mathrm{g}} - E}{\gamma_{\mathrm{opt}}/2}\right)^{5/4}\right) \tag{4.5}$$

$$\gamma^5{}_{\mathrm{opt}} = \left(\frac{e^2}{4\pi\varepsilon_{\mathrm{r}}\varepsilon_0}\right)^4 \frac{N^2{}_{\mathrm{t}}\hbar^2}{m_{\mathrm{r}}} \tag{4.6}$$

Similarly, solely bandgap variations can be modelled by converting E_g into a Gaussian distribution characterized by a mean bandgap ($\mathrm{E_{g,mean}}$) and a standard deviation (σ_{g}): [22]

$$\alpha \propto \int_0^\infty \frac{1}{\sigma_{\mathrm{g}}\sqrt{2\pi}} exp\left(-\frac{1}{2}\left(\frac{E_{\mathrm{g}} - E_{\mathrm{g,mean}}}{\sigma_{\mathrm{g}}}\right)^2\right) \times \left(\frac{\sqrt{E - E_{\mathrm{g}}}}{E}\right) dE_{\mathrm{g}} \tag{4.7}$$

Both models of equation 4.5 and equation 4.7 gave reasonable fits as shown in Figure 4.10 and Figure 4.11 respectively. Estimated parameters from both models are shown in Table 4.3.

Sample	γ_{opt} (meV)	N_t (cm^{-3})	σ_{g}(meV)
Reference	27.6	5.9×10^{18}	55.5
0.02M LiF	25.0	4.6×10^{18}	52.1
0.1M KF	26.9	5.5×10^{18}	56.9
0.01M RbF	22.3	3.5×10^{18}	48.4

Table 4.3: Estimation of amplitude of potential fluctuations (γ_{opt}), associated charged defect density (N_t) and standard deviation of a Gaussian variation in bandgap (σ_g).

The γ_{opt} values with Li-doping (25.0 meV) and Rb-doping (22.3 meV) may be compared with the 33 meV obtained by this model for a 11 % efficiency cell and 18 meV for a 5 % efficiency, silver based AZTSe cell [22, 42]. Using silver instead of copper in such a cell is aimed at reducing band tailing caused by Cu-Zn anti-site defects.

The charged defect densities (N_t) are also seen to reduce with Li and Rb doping as compared to the reference. They are all in the order of magnitude that is expected from other models [22, 33]. The experimentally determined relative dielectric constant of kesterite material is in the range from 8.5 for CZTSe and 6.7 for CZTS. These are significantly lower values than that of CIGS(e) (12) [2, 21]. This makes the material more susceptible to fluctuations due to charged defects and any reduction such as in Table 4.3 with Li and Rb doping is encouraging.

It should be emphasized that the models used here estimate either purely for bandgap fluctuations or electrostatic potential fluctuations. Recombination through tail states is likely a superposition of both phenomena.

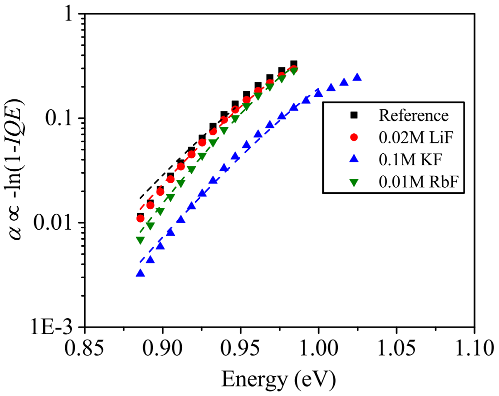

Figure 4.10: An analysis of absorption coefficient below the bandgap of each cell was used to quantify the density of charged defects which could cause electrostatic potential fluctuations in the conduction and valence bands.

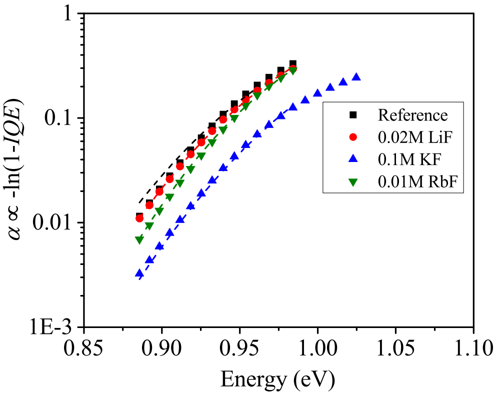

Figure 4.11: Absorption coefficient below the bandgap of each cell was fitted to estimate bandgap fluctuations assuming a Gaussian distribution of the bandgap.

4.6. Conclusions

In summary, a simple spin coating technique for introduction of alkali ions in CZTSe absorber was demonstrated. Statistical data was obtained from every device with 30 cells of 0.5 cm^2 in each case. The addition of Rb and Li in the presence of Na was seen to reduce bulk recombination and increases minority charge carrier lifetime to 6.8 ns and 8 ns, respectively. Rb doping showed the lowest difference (37 meV) between the photoluminescence peak and bandgap. Li-doping showed a clear increase in majority (hole) charge carrier density to the order of $10^{16}\,\mathrm{cm}^{-3}$. While maintaining the same bandgap, the V_{OC} deficit was lowered from 566 mV to 538 mV with Li doping. This highest achieved V_{OC} of 454 mV is 46 mV more than in the referred 9.7 % CZTSe cell. However, similar fill-factor and short-circuit current density are required for better efficiencies. Analyses of time-resolved photoluminescence and internal quantum efficiency showed evidence of tail states. Tail states were analyzed with models for electrostatic potential fluctuations and bandgap variations which suggest that band tailing may have been reduced by the addition of Li and Rb.

5

Ge based CZGSe

The work of this thesis was executed under the European Union's SWInG horizon 2020 project. The ultimate goal of this project is to develop a high bandgap solar cell/mini-module technology which can form the top part of a tandem solar cell. Tin and selenium based CZTSe were a starting point for it. A range of high bandgap materials can be created with the incorporation of germanium and sulphur, from 1.4 eV CZGSe to 1.9 eV CZGS with intermediate bandgaps stemming from CZGSSe [2]. As explained in chapter 2, there is also an incentive to partially or fully substitute tin in CZTSe as an excess of tin can create secondary phases such as $SnSe_2$ and a deficiency of Sn can create deep acceptor type defects (V_{Sn} and Cu_{Sn}). The volatility of tin and its compounds can also create reproducibility issues.

This chapter shows experiments performed for the development of CZGSe material in conjunction with the rest of the team at imec. Since this is the most recent work performed in this team, only a limited depth of analysis is presented here. Ongoing and future efforts in this team will be focused on CZGSSe and in particular, on the incorporation of sulphur.

5.1. Selection of a suitable substrate

Initial attempts at growing CZGSe on the standard SLG/Mo (400 nm) substrate ended with severe adhesion issues and small grain sizes. A possible reason for this is hypothesized to be the diffusion of sodium from the glass substrate. This normally has a positive effect on the performance of CIGS(e) and CZTSSe cells with regards to grain size, majority carrier concentration, bulk recombination and passivation of grain boundaries. A thorough testing of this hypothesis would be important for the scientific community since research groups are otherwise bound to dedicate time to testing the effects of sodium.

In the search for a suitable substrate, one with SLG/SiON/Mo (200 nm) and one with 700 µm of Si, 200 nm of SiO_2 (created via wet oxidation) and 400 nm sputtered molybdenum were tested. The former has a barrier to inhibit the diffusion of sodium, calcium and other elements from the glass and the latter is virtually free of impurity elements. Three cleaning durations of time with NH_4OH were also used on these substrates: 0 minutes, 6 minutes and 30 minutes. All substrates were then subject to e-beam evaporation of metal precursors and a subsequent selenium atmosphere annealing. A schematic of the original substrate and the new substrates is shown in Figure 5.1.

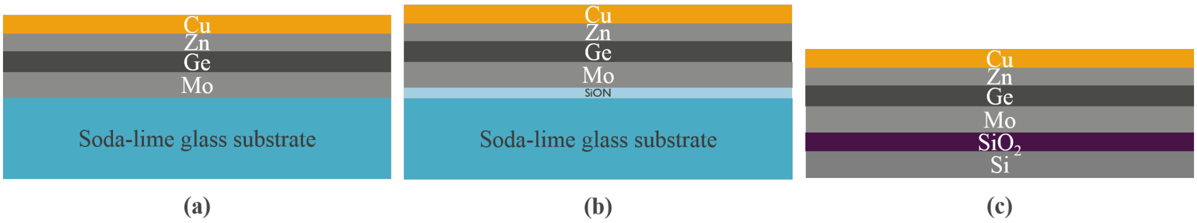

Figure 5.1: Three substrates were tested for the growth of CZGSe: (a) SLG/Mo (b) SLG/SiON/Mo (c) Si/SiO_2/Mo; and solar cells were succesfully created on (b) and (c).(Not to scale)

From an adhesion point of view, the cleaning step was observed to be extremely crucial and that 6 minutes seemed to be an optimal time. 30 minutes of cleaning lead to non-uniformity and a poor *PL* response.

The SLG/SiON/Mo substrate showed excellent cell results leading to the conclusion that a barrier was required to inhibit the diffusion of Na from the glass. This conclusion was further supported by the cell results on the Si/SiO$_2$/Mo substrate (Figure 5.2). It only required a 10 °C lower temperature of annealing due to the higher thermally conductivity of silicon as opposed to SLG. Subsequent experiments were conducted on the SLG/SiON/Mo substrate with 6 minutes of cleaning with NH$_4$OH. More Si/SiO$_2$/Mo substrates will also be used for experiments where a micro-meter thick substrate is required.

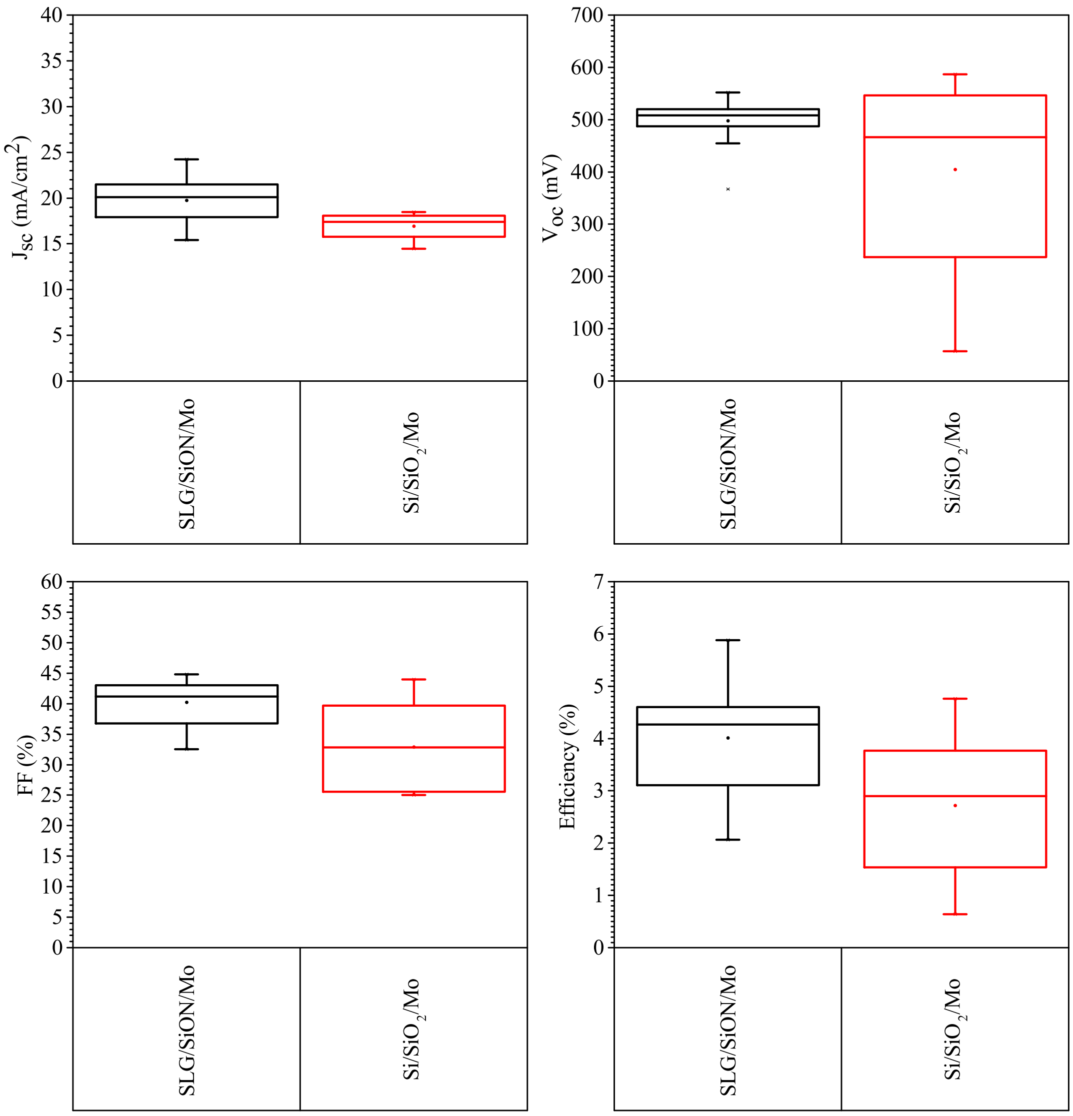

Figure 5.2: Cell results with different substrates suggest that diffusion of sodium from soda lime glass may have a negative impact on grain growth of CZGSe material.

A high efficiency of 5.9 % was achieved in these experiments, which is close to the state of the art for this material. The biggest opportunity for improvement seems to be in the carrier collection as J_{SC} values between 15 mA/cm^2 to 24 mA/cm^2 were observed. An optimization of the CdS buffer layer deposition conditions was required for all samples, especially with respect to temperature. In the external quantum efficiency (*EQE*) of the Si/SiO$_2$/Mo substrate sample shown in Figure 5.3, we can observe an overall low response (80 %) but an especially low response (< 60 %) below 500 nm which can be due to parasitic absorption in CdS (bandgap 2.42 eV or 517 nm).

An XRD analysis of the absorber on the Si/SiO$_2$/Mo substrate confirmed that in the crystalline phases

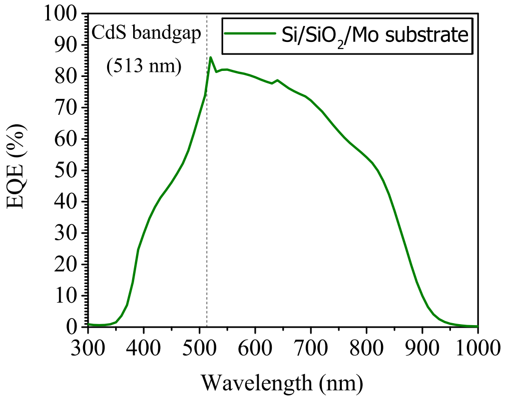

Figure 5.3: External quantum efficiency (*EQE*) of a CZGSe cell on a Si/SiO$_2$/Mo susbtrate shows the need for better carrier collection across all wavelengths and for reduction of parasitic absorption from CdS..

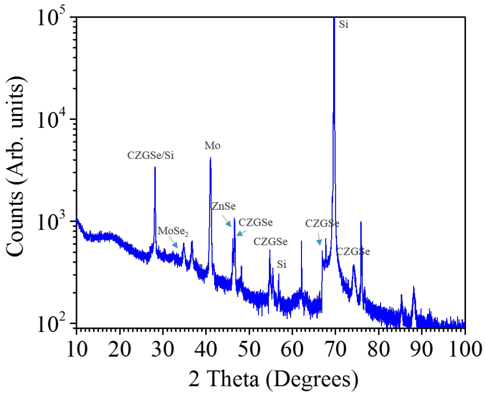

Figure 5.4: XRD analysis showed that CZGSe was the dominant crystalline phase formed, followed by ZnSe and MoSe$_2$.

observable, CZGSe was dominant. Some traces of ZnSe and MoSe2 were also seen (Figure 5.4).

5.2. Effects of absorber thickness

Different absorber thicknesses were tested in order to study whether the dominant recombination mechanism in CZGSe is in the bulk or at the interfaces. Three precursor thickness were used, as shown in Table 5.1. They covered a 50 % increase or decrease in the thickness of metal precursors used, with respect to a set reference.

Device	Ge (nm)	Zn (nm)	Cu (nm)
Thin device	119	87	126
Reference device	180	125	170
Thick device	270	187	255

Table 5.1: Different metal precursor thicknesses very tested to study the behaviour of recombination in the bulk/interfaces.

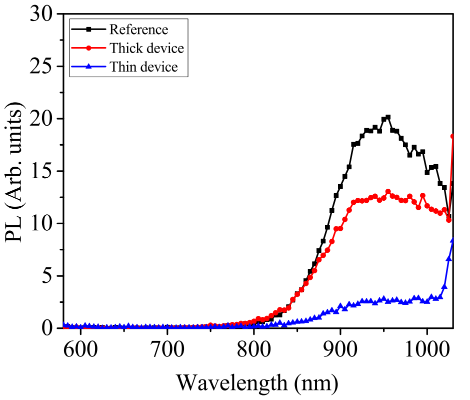

Figure 5.5: Thicker CZGSe layers showed a photoluminescence response while the thinner one did not.

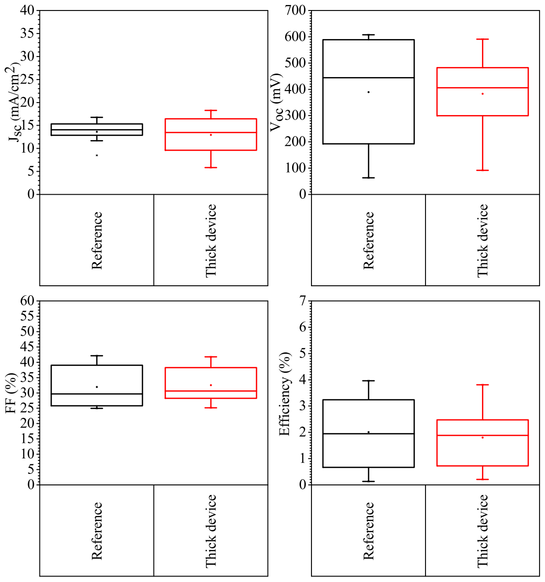

Figure 5.6: Similar electrical performance was observed despite an increase of 50 % in Ge, Zn and Cu precursor thicknesses.

Photoluminescence (PL) analysis showed that the reference and thick device had the expected response but the thin device did not (Figure 5.5). The latter was therefore not processed for cell results as the metal precursors were probably too thin to create sufficient CZGSe. In the cell results, similar performance was observed in either device, even though the thicker device had 50 % more Ge, Zn and Cu (Figure 5.6). As in the results of the previous section, the J_{SC} is low in either device, leaving ample room for improvement.

5.3. Search for a chemical etch

The formation of a quaternary compound semiconductor is always in competition with other binary and ternary compounds, depending on their relative enthalpy of formation. A suitable etchant can be useful in removing secondary phases accumulated at the surfaces. Metal precursors are often engineered (as in this work) in terms of quantity and position, in order to induce the formation of desired compounds. The etch step can assist in further optimization of the stoichiometry. In addition, it may also passivate bonds or defects on the surface. It is known from previous studies, that both KCN and the relatively less toxic $(NH_4)_2S$, can be suitable etchants for CZTSe. One major difference being that $(NH_4)_2S$ needs approximately double the etch time as KCN [43]. Thus, a similar experiment was executed on CZGSe with a KCN etch of 6 minutes and a $(NH_4)_2S$ etch of 12 minutes.

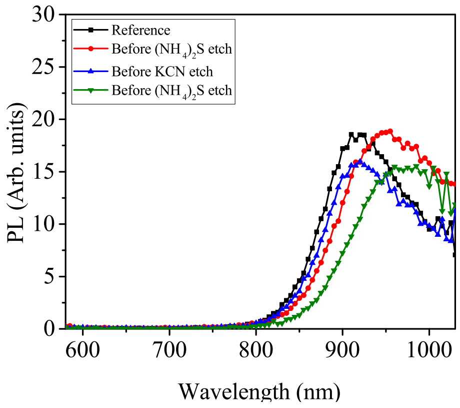

Figure 5.7: Photoluminescence response of CZGSe devices after selenium-atmosphere annealing.

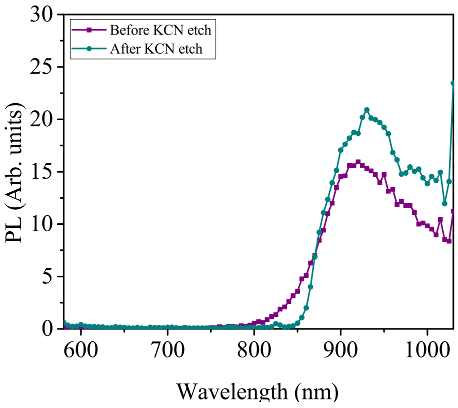

Figure 5.8: Increase in photoluminescence response after KCN etch of 6 minutes.

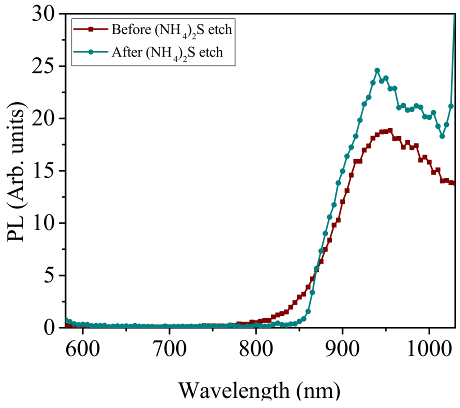

Figure 5.9: Increase in photoluminescence response after $(NH_4)_2S$ etch of 12 minutes.

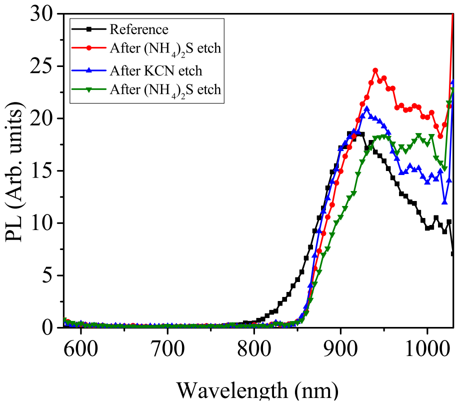

Figure 5.10: Final photoluminescence response of devices which were processed into solar cells.

Figure 5.7 shows the *PL* response of all devices after the selenium-atmosphere annealing. There are some variations already present here with the reference device having a high and narrow *PL* peak. Non-uniformity was also observed at different spots on any given sample. Nevertheless, an increase in *PL* response was observable with a KCN etch (Figure 5.8) as well as an $(NH_4)_2S$ etch (Figure 5.9). This is an encouraging result and warrants a more detailed study in the future with advanced techniques such as inductively coupled plasma atomic emission spectroscopy (ICP-AES) and X-ray photoelectron spectroscopy (XPS). Uniformity within the devices also needs to be improved for a better study.

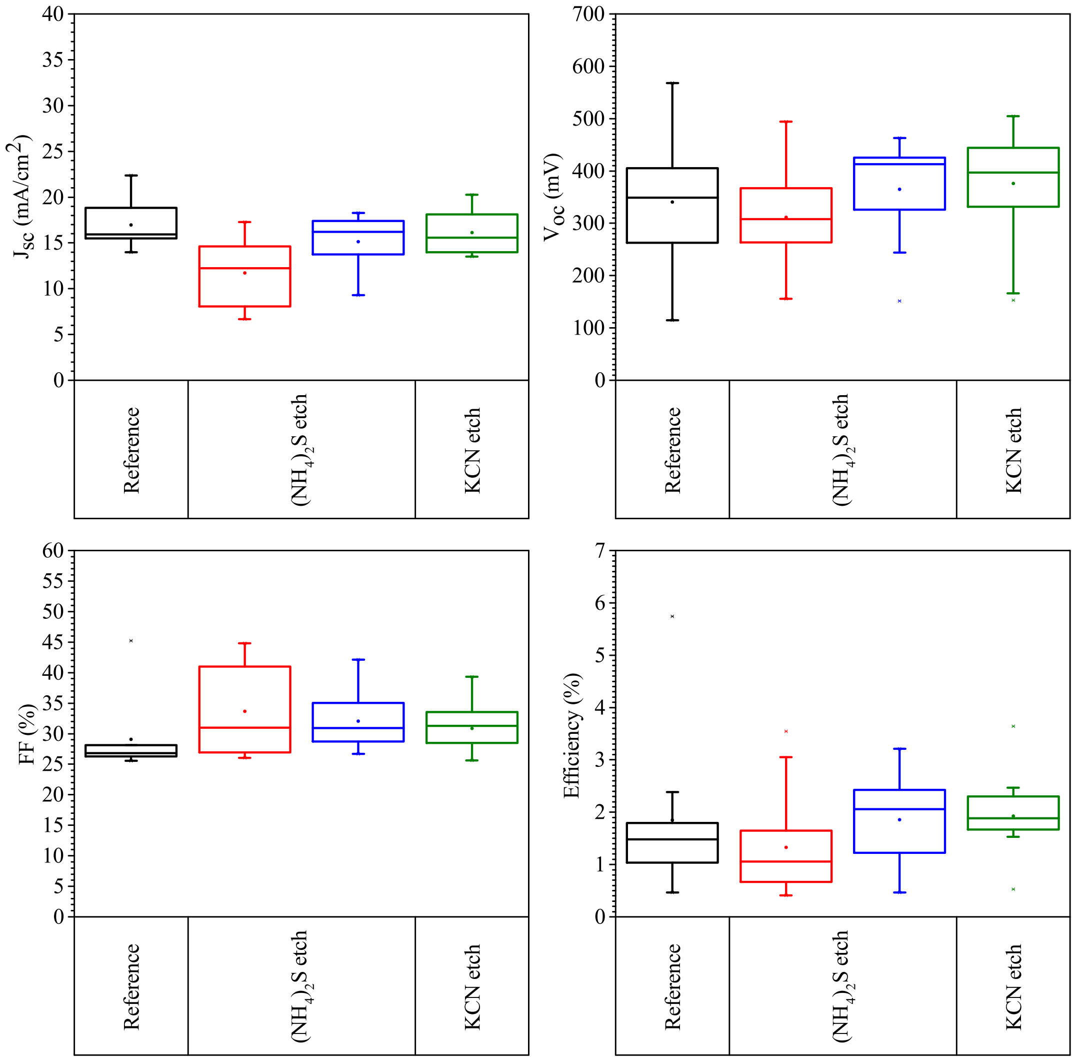

Figure 5.11: Statistics over 14 cells on each device suggest that etching with $(NH_4)_2S$ or KCN could improve cell performance.

Figure 5.10 shows the final *PL* response after the respective etch steps, along with the reference which received no chemical treatment. These devices were processed further to make complete solar cells. The result of their electrical characterization is shown in Figure 5.11. The mean and median values suggest that both $(NH_4)_2S$ and KCN could improve cell performance as compared to the reference, but neither of them gave the 6 % efficiency expected from the present fabrication steps. This is evident from the outlier cell in the reference which was the only one to show 5.7 % efficiency. As mentioned earlier, an improvement in the uniformity of CZGSe formation and an optimization of CdS deposition conditions seems required.

5.4. Conclusion

The diffusion of sodium and other elements from soda lime glass substrates seem to have a negative effect on the adhesion of $Cu_2ZnGeSe_4$ material and its grain size. A suitable substrate with a SiON barrier for this purpose was identified. Si wafer based substrates with SiO_2 and molybdenum were also found to be suitable and will be used for experiments where micro-meter thin substrates are required. The cleaning of these substrates with 30 wt% NH_4OH for 6 minutes was also found to be important for adhesion.

Etching of the absorber with KCN or $(NH_4)_2S$ showed an increase in photoluminescence response. This can be investigated further especially if different metal stack configurations, annealing parameters and dopants are tested and a removal of unwanted compounds or a passivation of exposed surfaces with sulphur is desired.

The highest solar cell efficiency achieved was 5.9 % which is close to the state of the art for this technology. It was noticed that an optimization of the CdS buffer layer deposition conditions is essential to obtain good cell results. A modification of gas flow in the selenium-atmosphere annealing step is also required to obtain more uniformity in the photoluminescence response within a device.

6

Front surface passivation

If the performance of a solar cell is limited by its interfaces more than its bulk, then certain steps can be taken for improvement:

1. **An increase in the thickness of the absorber**, so that more charge separation occurs before recombination at a surface

2. **A chemical etch** of the absorber to remove unwanted compounds/impurities and passivate dangling bonds or defects

3. **Deposition of a passivation layer** to chemically and/or electrically passivate the surface of an absorber layer and reduce recombination at that interface.

High power conversion efficiencies in crystalline silicon solar cells have been achieved through the invention of complex cell architectures such as PERC (passivated emitter and rear cell) and PERL (passivated emitter rear locally-diffused). Such concepts have been recently demonstrate on CIGS(e) solar cells too [44]. Passivation layers can generally lead to better carrier collection (J_{SC}) or in the best cases, even an improvement in open-circuit voltage (V_{OC}). However, they have be optimally thin or have adequate openings in order to avoid an increase in series resistance.

In the work on kesterite (CZTSe) solar cells at imec, improvements have been made via an increase in the absorber thickness, optimized chemical etch with KCN or $(NH_4)_2S$ and passivation at the Mo/CZTSe interface with MoO_3 and Al_2O_3 [30, 31, 43, 45, 46]. The next logical step therefore, was to find a suitable material for passivation of the top surface which is the CZTSe/CdS interface. Atomic layer deposition was chosen as the deposition technique since it is the most suitable method to grow ultra-thin layers (<10 nm) and can provide highly conformal coverage on rough surfaces. Existing literature suggests that Al_2O_3 grown via ALD is a promising solution for the passivation of defects of compound semiconductors [47–49].

6.1. Deposition on front surface

The typical growth rate of Al_2O_3 at 150 °C is 0.11 nm/cycle. It is actually well below 1 atomic monolayer of growth per cycle. This is because of steric hindrances or non-uniform surface reactivity on the atomic scale. Nevertheless, with enough number of cycles (i.e > 4 cycles), no gaps are left in the deposited layers and highly conformal, uniform growth can be expected. In terms of deposition on different surfaces, such as CZTSe instead of silicon, the first nucleation layer is important. Once that is achieved, subsequent layers will grow on top of it and with a growth rate close to 0.11 nm/cycle. This makes ALD an extremely attractive technique for practical applications.

For the experiments presented in this chapter, different devices were subjected to various numbers of ALD cycles. As an illustration, Figure 6.1 shows a CZTSe absorber on the left and a clearly visible Al_2O_3 layer on top of a CZTSe absorber on the right. This sample was subjected to 258 cycles of ALD, which would give 30 nm of Al_2O_3 on a clean silicon wafer. Similarly, the ALD layer thicknesses shown in the results of this chapter are ideal growth numbers and only indicative of the range of thickness of the layers.

All devices were processed together except for the TCO deposition, where two devices (with 43 cycles and 151 cycles) were subjected to a lower temperature of deposition. The effect of this difference is negligible after the 200 °C O_2 atmosphere annealing step. It is; however, important for the data in Figure 6.4 and is highlighted again in the discussion of the results.

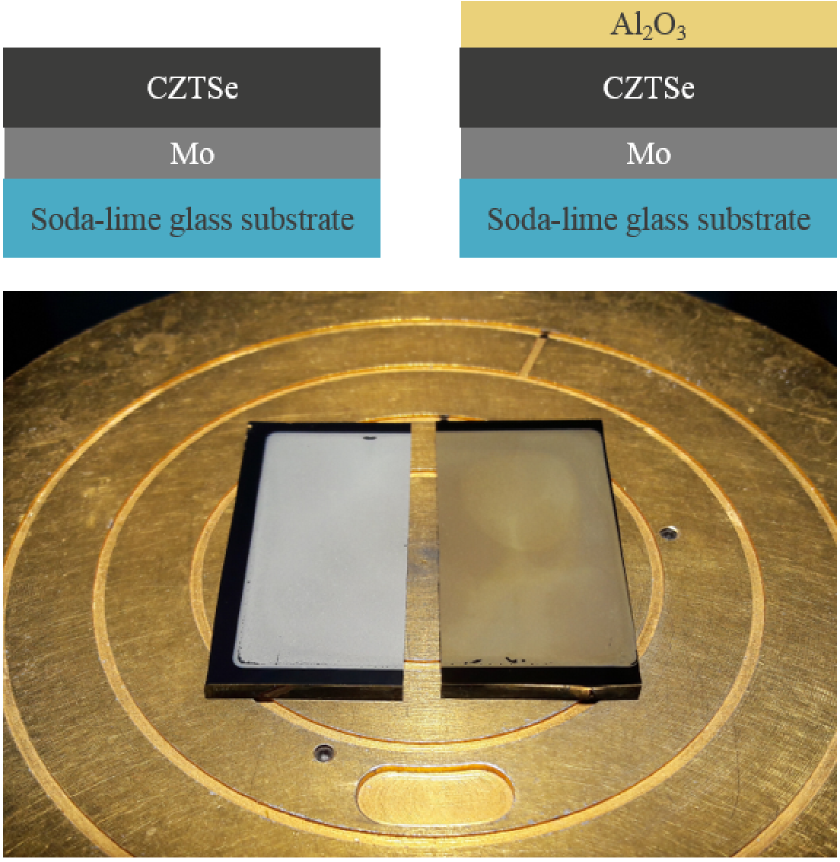

Figure 6.1: Al_2O_3 was deposited via ALD on the top surface of CZTSe in the solar cell architecture.

The deposition of a CdS buffer layer was done after the ALD step, as described in chapter 2. NH_4OH is one of the reactants in the solution to form CdS, which is also known to etch Al_2O_3 [50]. It is therefore expected that a residual amount of NH_4OH present in the solution will etch the Al_2O_3 during the deposition time of 6 to 8 minutes. Since the concentration of the residual NH_4OH was not know, an exact calculation of the etched amount could not be made. These layers are also below the resolution limit of scanning electron microscopy (SEM). Therefore, layers as thick as 17.5 nm were used.

6.2. Photoluminescence studies

To study the effect of the deposition on the absorber, photoluminsence (*PL*) measurements were done on the bare absorbers, after KCN etch and after the oxide deposition. The *PL* response of an absorber reduces after the KCN etch. The exact reason for this phenomena is still under study but it is acknowledged that despite this, the KCN etch has a positive effect on the performance of the absorber [31]. The *PL* response is normally recovered after the CdS and TCO deposition and O_2/N_2 atmosphere annealing.

In Figure 6.2, we can see that the *PL* response can also be recovered after ALD deposition of Al_2O_3. There was no recovery in the case of the reference. The *PL* response was seen to increase with an increasing number of ALD cycles. This is a positive sign for the amount of radiative recombination in the bulk. A question arises; however, whether this increase is due to a passivation of the top surface by Al_2O_3 or by the heat of the ALD chamber at 150 °C. This is discussed further in the last section.

6.3. Solar cell results - a critical view

The complete set of electrical parameters (J_{SC}, V_{OC}, *FF* and efficiency) for this data set are shown in Figure 6.3. Each device in this experiment was of the dimensions, 2.5 cm × 5 cm and with 10 to 16 cells each. Higher

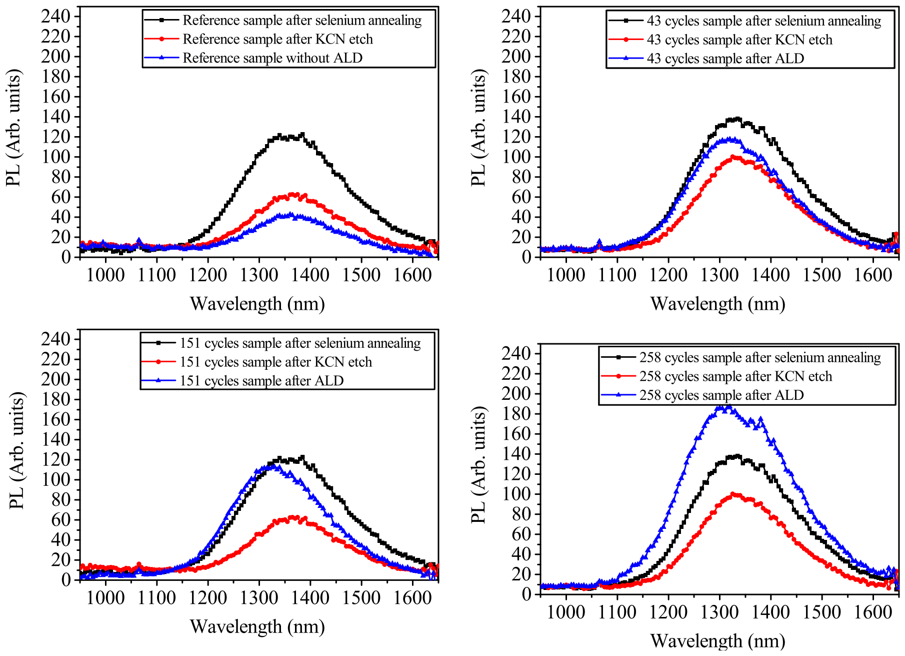

Figure 6.2: Photoluminescence response of CZTSe increases with an increasing number of ALD cycles.

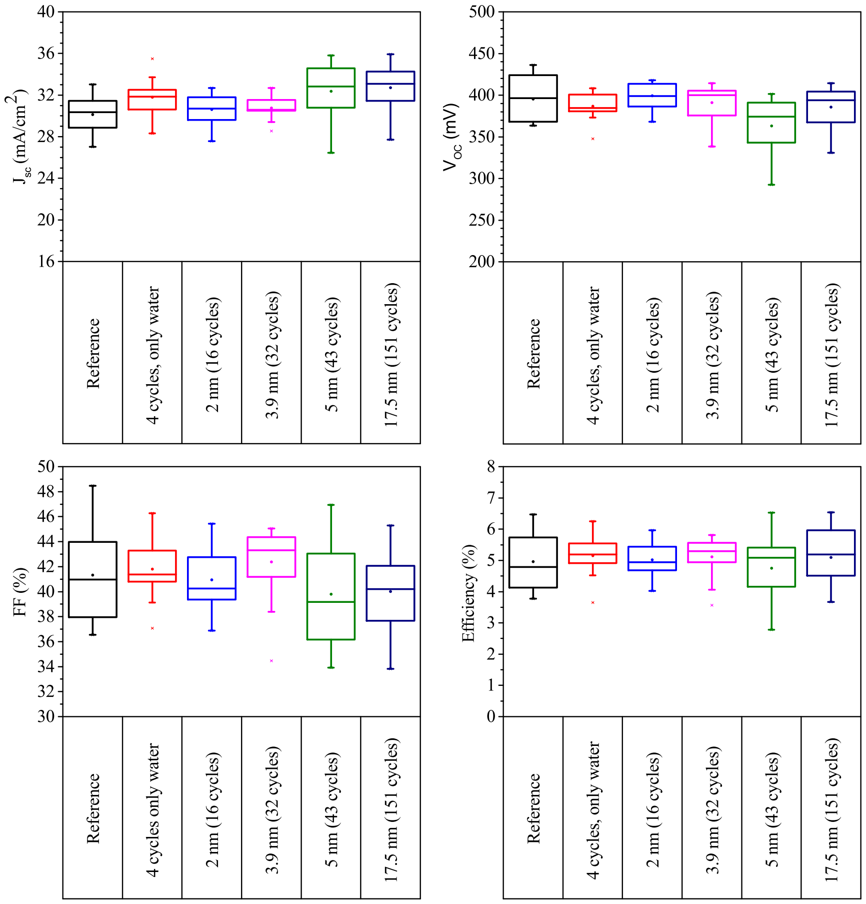

Figure 6.3: Electrical parameters of all working cells in the ALD Al_2O_3 experiment showed an increasing trend in J_{SC} but similar efficiencies overall.

cycles of ALD, showed improved carrier collection in mean, median and top 25 % quartile in J_{SC}. The highest value of J_{SC} achieved was 36 mA/cm^2. Overall, no significantly higher efficiency was achieved. The trend in the J_{SC} is interesting and warrants further analysis. The Al_2O_3 layer thickness values are as expected after deposition on a silicon wafer. They are only indicative of the deposition and are probably not the final layer thickness values due to reasons discussed in the first section.

The O_2/N_2 atmosphere annealing at 200 °C is now a standard step in the cell fabrication process. In all the experiments presented in this thesis, a performance improvement was seen with the annealing step. In this particular experiment, the ALD deposition was done at 150 °C, which creates an additional heating step in the cell fabrication process. The duration of the step varies vastly for each device since 1 ALD cycle takes approximately 5 minutes. Therefore, a cell may undergo heat exchange for 0 minutes (reference), 20 minutes (4 cycles) or up to 4.5 hours (258 cycles).

The ALD temperature of 150 °C is lower than the predicted 200 °C critical temperature for order/disorder transitions in CZTSe. Nevertheless, it's effect cannot be discounted. Bourdais et al., have shown in their experiments to thermally create order/disorder, that devices cooled in a relatively fast manner have around 40 mV lower V_{OC} and 1.8 mA/cm^2 more J_{SC} than slowly cooled samples [2]. In other words, the effect of the temperature of the ALD process may have a significant impact on order/disorder in the kesterite material and accordingly V_{OC} and carrier collection.

6.4. Thermal budget of CZTSe

To understand the effect of this heating, two steps were taken. One was to include a device which is only subject to 20 minutes of heating, and no formation of an Al_2O_3 layer (shown in Figure 6.3). It was subject to four water precursor pulses, but not to the TMA precursor. The other step was to characterize solar cells before and after the 200 °C annealing step.

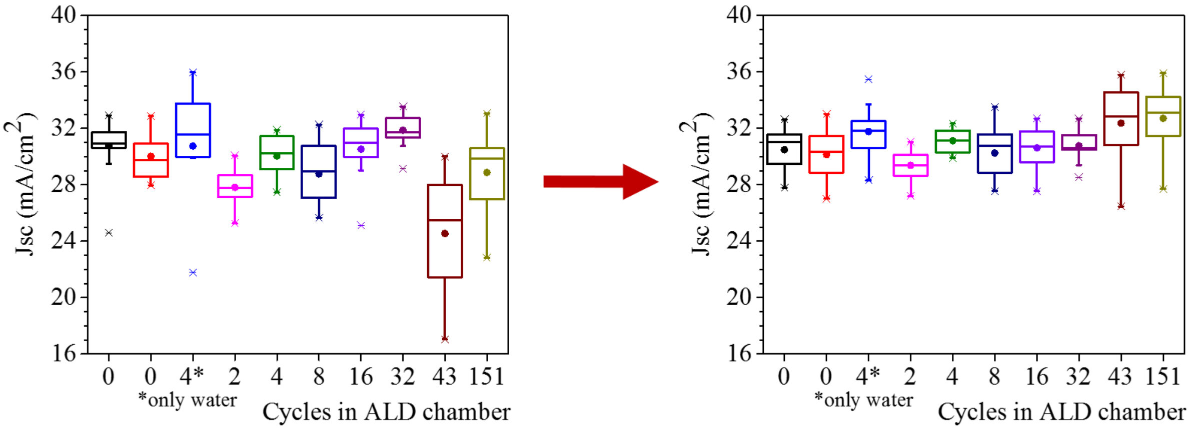

Figure 6.4: Electrical characterization before and after the 200 °C annealing step suggest that the temperature of the ALD process affects cell performance as much or more than the Al_2O_3 layer itself.

Before the 200 °C annealing step, an increasing trend was seen in the J_{SC} values with increasing duration in the ALD chamber (left side of Figure 6.4). The devices subjected to 43 and 151 cycles of ALD show a change in this trend because they were subjected to a lower temperature of TCO deposition than the other devices. This was unavoidable as the deposition had to be done together with other CZGSe based devices.

After the 200 °C annealing step, these differences tended to equalize, as visible in the right of Figure 6.4. The device that was subject to only water precursors pulses gives more support to a conclusion that the heating steps creates as much difference in the final cell performance as an Al_2O_3 layer. The performance of the solar cells is therefore, still dominated by the bulk.

Since the ALD process is extremely sensitive to the temperature of the precursors and substrates, lower deposition temperature of Al_2O_3 is only possible with plasma-enhancement techniques. If 150 °C is indeed a temperature which can drastically affect the performance of kesterite cells, then this raises serious questions on the thermal budget such a technology would have for large volume production.

7

Conclusion and outlook

7.1. Concluding remarks

This thesis was a unique opportunity to study and develop novel thin-film solar cells of the $Cu_2Zn(Ge,Sn)Se_4$ family of materials. Since these are relatively new materials and there is limited understanding of their behaviour, two sets of experiments were made specifically on the semiconductor material. A third set of experiments attempted to add a new passivation layer in the cell architecture via atomic layer deposition.

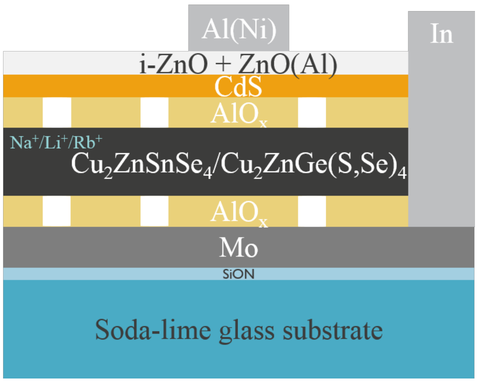

Figure 7.1: Schematic showing various aspects investigated and recommended in this thesis.

In chapter 4, a simple, non-vacuum spin-coating technique was demonstrated for the addition of Li^+, K^+ and Rb^+ to $Cu_2ZnSnSe_4$ absorber material. The highest open-circuit voltage (V_{OC}) achieved with the addition of Li^+ was 454 mV which is among the highest recorded V_{OC} for $Cu_2ZnSnSe_4$ technology [2]. A V_{OC} of 441 mV was also achieved with Rb^+ doping. These ions were shown to reduce bulk recombination and increase minority charge carrier decay time to 6.8 ns (with Rb^+) and 8 ns (with Li^+). Rb doping showed the lowest difference (37 meV) between the photoluminescence peak and bandgap. Li-doping showed a clear increase in majority (hole) charge carrier density to the order of 10^{16} cm^{-3}. A detailed analysis of diode characteristics, photoluminescence and *IQE* suggested a reduction in shallow states below the bandgap. Along with these improvements, it was noted that higher fill-factor and short-circuit current are required to achieve record efficiencies.

The results and analysis approach used in this work are of significant importance to the scientific community, since V_{OC} deficit has been identified as a critical bottleneck for kesterite $Cu_2ZnSn(S,Se)_4$ technology in recent years. The best bandtailing factor acquired from the model for electrostatic potential fluctuations was 22.3 meV with Rb-doping. It can be compared with the 33 meV for a 11 % efficiency $Cu_2ZnSn(S,Se)_4$ cell and 18 meV for a 5 % efficiency $Ag_2ZnSnSe_4$ cell, also obtained with the same model [22, 42]. In the latter, Cu/Zn type disorders are expected to be significantly lower due to the difference in ionic radii of silver and zinc. This work was presented in a poster format at the European Materials Research Society's spring 2017 conference and is currently under review for publication as a manuscript in Physica Solidi Status journals.

Chapter 5 shows the results of experiments in the development of $Cu_2ZnGeSe_4$ solar cells, motivated by tandem solar cell applications and the elimination of Sn based defects, secondary phases and reproducibility issues. Two appropriate substrates and a cleaning step were identified for the successful growth of this material. Etching with KCN and the less toxic $(NH_4)_2S$, both showed potential to improve results via the removal of secondary compounds from surfaces or passivation of dangling bonds by sulphur. Among all these experiments, the highest solar efficiency achieved was 5.9 % which is close to the state of the art for this material. Future efforts of the 'Alternative Thin-film PV' group at imec will be focused on the incorporation of sulphur to create $Cu_2ZnGe(S,Se)_4$ solar cells with a bandgap of 1.6-2.1 eV and efficiency close to 15 %.

The work in chapter 6 showcases efforts to create a Al_2O_3 passivation layer between kesterite material and CdS buffer layer, via atomic layer deposition. In these attempts to reduce recombination at the surface, the highest short circuit current density achieved was 36 mA/cm^2. However, evidence was presented for this improvement possibly also arising from the 150 °C temperature of the ALD process. The performance of these kesterite solar cells was concluded to still be heavily dominated by the bulk. Initial results of this work were presented in a poster at the European Kesterite workshop in November 2016. A similar passivation technique with GaO_x on CIGS(e) was also characterized and will be submitted for publication in the near future.

7.2. Outlook

For future work on these materials, the addition of Li^+ and Rb^+ to $Cu_2ZnSnSe_4$ show promise in reducing V_{OC} deficit. A major breakthrough could be achieved just as in the case of potassium and rubidium based post-deposition treatment of CIGS(e) solar cells which have given efficiencies up to the world record of 22.6 % [14]. Likewise, germanium based alloying has also shown great potential in carrying this technology forward [27]. Other possible solutions to reduce sub-bandgap absorption include the incorporation of cadmium for an increase in the dielectric constant or the replacement of copper with silver to reduce I-II type disorder. Cadmium's toxicity and silver's rarity remove the advantages sought from kesterite materials, but provide more evidence to the theoretical understanding of kesterite material.

In the development of high bandgap $Cu_2ZnGe(S,Se)_4$ for tandem solar cells, barriers will be required to inhibit the diffusion of sodium, calcium and other elements from glass substrates (as shown in Figure 7.1). Etching with KCN and $(NH_4)_2S$ can be explored again with advanced characterization techniques such as inductively coupled plasma atomic emission spectroscopy (ICP-AES) and X-ray photoelectron spectroscopy (XPS).

Atomic layer deposition can certainly become an effective and popular passivation technique for various type of solar cell materials due to its highly conformal growth, soft deposition and ease of growth over chemically different substrates. High resolution ellipsometry and other advanced techniques will be required to characterize ultra-thin (<10 nm) layers. Thick passivation layers could also be made, if sufficiently large contact openings are created for the flow of charge. This is illustrated in Figure 7.1. As a final word of caution, it would also be advisable to investigate the thermal budget of $Cu_2Zn(Ge,Sn)(S,Se)_4$ based solar cells before efforts are made for large scale production.

Bibliography

[1] David B Mitzi, Oki Gunawan, Teodor K Todorov, and D Aaron R Barkhouse. Prospects and performance limitations for Cu-Zn-Sn-S-Se photovoltaic technology. *Philosophical Transactions of the Royal Society of London A: Mathematical, Physical and Engineering Sciences*, 371(1996):20110432, 2013.

[2] Stéphane Bourdais, Christophe Choné, Bruno Delatouche, Alain Jacob, Gerardo Larramona, Camille Moisan, Alain Lafond, Fabrice Donatini, Germain Rey, Susanne Siebentritt, et al. Is the Cu/Zn disorder the main culprit for the voltage deficit in kesterite solar cells? *Advanced Energy Materials*, 6(12), 2016.

[3] NASA. Image of vanguard 1 satellite. URL `https://www.hq.nasa.gov/office/pao/History/sputnik/vanguard.jpg`. [Online; accessed 13-June-2017].

[4] Shiyou Chen, Aron Walsh, Xin-Gao Gong, and Su-Huai Wei. Classification of lattice defects in the kesterite Cu_2ZnSnS_4 and $Cu_2ZnSnSe_4$ earth-abundant solar cell absorbers. *Advanced Materials*, 25(11): 1522–1539, 2013.

[5] Jatosado. Schematic of a electron beam physical vapor deposition system. URL `https://en.wikipedia.org/wiki/Electron_beam_physical_vapor_deposition#/media/File:Electron_Beam_Deposition_001.jpg`. [Online; accessed 23-June-2017].

[6] HCM Knoops, SE Potts, AA Bol, and WMM Kessels. Atomic layer deposition. 2015.

[7] Taesoo D Lee and Abasifreke U Ebong. A review of thin film solar cell technologies and challenges. *Renewable and Sustainable Energy Reviews*, 2016.

[8] Fraunhofer ISE. Photovoltaics report. Technical report, Freiburg, June 2016.

[9] Solar Power Europe (SPE). Global market outlook for solar power 2015-2019. report, June 2015.

[10] Fraunhofer ISE. Current and future cost of photovoltaics—long-term scenarios for market development, system prices and LCOE of utility-scale PV systems. report, February 2015.

[11] Colin A Wolden, Juanita Kurtin, Jason B Baxter, Ingrid Repins, Sean E Shaheen, John T Torvik, Angus A Rockett, Vasilis M Fthenakis, and Eray S Aydil. Photovoltaic manufacturing: Present status, future prospects, and research needs. *Journal of Vacuum Science & Technology A: Vacuum, Surfaces, and Films*, 29(3):030801, 2011.

[12] William Shockley and Hans J. Queisser. Detailed balance limit of efficiency of pn junction solar cells. *Journal of Applied Physics*, 32(3):510–519, 1961. doi: 10.1063/1.1736034. URL `http://dx.doi.org/10.1063/1.1736034`.

[13] Martin A Green. Third generation photovoltaics: advanced solar energy conversion. *Physics Today*, 57 (12):71–72, 2004.

[14] Philip Jackson, Roland Wuerz, Dimitrios Hariskos, Erwin Lotter, Wolfram Witte, and Michael Powalla. Effects of heavy alkali elements in Cu(In,Ga)se2 solar cells with efficiencies up to 22.6%. *physica status solidi (RRL) – Rapid Research Letters*, 10(8):583–586, 2016. ISSN 1862-6270. doi: 10.1002/pssr.201600199. URL `http://dx.doi.org/10.1002/pssr.201600199`.

[15] Fraunhofer ISE. Multicrystalline silicon solar cell with 21.9 percent efficiency: Fraunhofer ISE again holds world record, 2017. URL `https://goo.gl/W5POQk`. [Online; accessed 8-June-2017].

[16] K.Barbalace. Periodic table of elements 1995-2016. URL `http://EnvironmentalChemistry.com/yogi/periodic/In.html`. [Online; accessed 30-August-2016].

[17] European Commission. Communication from the commission to the european parliament, the council, the european economic and social committee and the committee of the regions, on the review of the list of critical raw materials for the eu and the implementation of the raw materials initiative. URL `https://ec.europa.eu/growth/sectors/raw-materials/specific-interest/critical_en`. [Online; accessed 12-June-2017].

[18] Wei Wang, Mark T. Winkler, Oki Gunawan, Tayfun Gokmen, Teodor K. Todorov, Yu Zhu, and David B. Mitzi. Device characteristics of CZTSSe thin-film solar cells with 12.6% efficiency. *Advanced Energy Materials*, 4(7):1301465–n/a, 2014. ISSN 1614-6840. doi: 10.1002/aenm.201301465. URL `http://dx.doi.org/10.1002/aenm.201301465`. 1301465.

[19] Hongxia Wang. Progress in thin film solar cells based on Cu_2ZnSnS_4. *International journal of Photoenergy*, 2011, 2011.

[20] Yun Seog Lee, Talia Gershon, Teodor K. Todorov, Wei Wang, Mark T. Winkler, Marinus Hopstaken, Oki Gunawan, and Jeehwan Kim. Atomic Layer Deposited Aluminum oxide for interface passivation of $Cu_2ZnSn(S,Se)_4$ thin-film solar cells. *Advanced Energy Materials*, 6(12):n/a–n/a, 2016. ISSN 1614-6840. doi: 10.1002/aenm.201600198. URL `http://dx.doi.org/10.1002/aenm.201600198`. 1600198.

[21] Guy Brammertz, M Buffière, S Oueslati, H ElAnzeery, Khaled Ben Messaoud, S Sahayaraj, Ch Köble, Marc Meuris, and Jef Poortmans. Characterization of defects in 9.7% efficient $Cu_2ZnSnSe_4$-CdS-Zno solar cells. *Applied Physics Letters*, 103(16):163904, 2013.

[22] Tayfun Gokmen, Oki Gunawan, Teodor K Todorov, and David B Mitzi. Band tailing and efficiency limitation in kesterite solar cells. *Applied Physics Letters*, 103(10):103506, 2013.

[23] Susan Schorr. The crystal structure of kesterite type compounds: A neutron and x-ray diffraction study. *Solar Energy Materials and Solar Cells*, 95(6):1482–1488, 2011.

[24] BG Mendis, MD Shannon, MCJ Goodman, JD Major, AA Taylor, DP Halliday, and K Durose. The nature of electrostatic potential fluctuations in Cu_2ZnSnS_4 and their role on photovoltaic device performance. In *Journal of Physics: Conference Series*, volume 471, page 012014. IOP Publishing, 2013.

[25] Germain Rey, Alex Redinger, Jan Sendler, Thomas Paul Weiss, Maxime Thevenin, M Guennou, B El Adib, and Susanne Siebentritt. The band gap of $Cu_2ZnSnSe_4$: Effect of order-disorder. *Applied Physics Letters*, 105(11):112106, 2014.

[26] Gerardo Larramona, Sergiu Levcenko, Stéphane Bourdais, Alain Jacob, Christophe Choné, Bruno Delatouche, Camille Moisan, Justus Just, Thomas Unold, and Gilles Dennler. Fine-tuning the Sn content in CZTSSe thin films to achieve 10.8% solar cell efficiency from spray-deposited water-ethanol-based colloidal inks. *Advanced Energy Materials*, 5(24), 2015.

[27] Sergio Giraldo, Thomas Thersleff, Gerardo Larramona, Markus Neuschitzer, Paul Pistor, Klaus Leifer, Alejandro Pérez-Rodríguez, Camille Moisan, Gilles Dennler, and Edgardo Saucedo. $Cu_2ZnSnSe_4$ solar cells with 10.6% efficiency through innovative absorber engineering with Ge superficial nanolayer. *Progress in Photovoltaics: Research and Applications*, 24(10):1359–1367, 2016.

[28] Mirjana Dimitrievska, Andrew Fairbrother, Edgardo Saucedo, Alejandro Pérez-Rodríguez, and Victor Izquierdo-Roca. Secondary phase and Cu substitutional defect dynamics in kesterite solar cells: Impact on optoelectronic properties. *Solar Energy Materials and Solar Cells*, 149:304–309, 2016.

[29] Marie Buffière, Guy Brammertz, Abdel-Aziz El Mel, Nicolas Barreau, Marc Meuris, and Jef Poortmans. Effect of ammonium sulfide treatments on the surface properties of $Cu_2ZnSnSe_4$ thin films. *Thin Solid Films*, 2016.

[30] Samaneh Ranjbar, Guy Brammertz, Bart Vermang, Afshin Hadipour, M Sylvester, Aniket Mule, Marc Meuris, AF da Cunha, and Jef Poortmans. Effect of Sn/Zn/Cu precursor stack thickness on two-step processed kesterite solar cells. *Thin Solid Films*, 2016.

[31] Marie Buffiere, Guy Brammertz, Sylvester Sahayaraj, Maria Batuk, Samira Khelifi, Denis Mangin, Abdel-Aziz El Mel, Ludovic Arzel, Joke Hadermann, Marc Meuris, et al. KCN chemical etch for interface engineering in $Cu_2ZnSnSe_4$ solar cells. *ACS applied materials & interfaces*, 7(27):14690–14698, 2015.

[32] Steven S Hegedus and William N Shafarman. Thin-film solar cells: device measurements and analysis. *Progress in Photovoltaics: Research and Applications*, 12(2-3):155–176, 2004.

[33] By Talia Gershon, Yun Seog Lee, Ravin Mankad, Oki Gunawan, Tayfun Gokmen, Doug Bishop, Brian McCandless, and Supratik Guha. The impact of sodium on the sub-bandgap states in CZTSe and CZTS. *Applied Physics Letters*, 106(12):123905, 2015.

[34] Xiaolei Liu, Yu Feng, Hongtao Cui, Fangyang Liu, Xiaojing Hao, Gavin Conibeer, David B Mitzi, and Martin Green. The current status and future prospects of kesterite solar cells: a brief review. *Progress in Photovoltaics: Research and Applications*, 2016.

[35] G Rey, F Babbe, TP Weiss, H Elanzeery, M Melchiorre, N Valle, B El Adib, and S Siebentritt. Post-deposition treatment of $Cu_2ZnSnSe_4$ with alkalis. *Thin Solid Films*, 2016.

[36] Elaheh Ghorbani, Hossein Mirhosseini, Janos Kiss, and Claudia Felser. Incorporation of li dopant into $Cu_2ZnSnSe_4$ photovoltaic absorber: hybrid-functional calculations. *Journal of Physics D: Applied Physics*, 48(48):482001, 2015.

[37] Yao-Tsung Hsieh, Qifeng Han, Chengyang Jiang, Tze-Bin Song, Huajun Chen, Lei Meng, Huanping Zhou, and Yang Yang. Efficiency enhancement of $Cu_2ZnSn(S, Se)\ _4$ solar cells via alkali metals doping. *Advanced Energy Materials*, 2016.

[38] Susanne Siebentritt, Germain Rey, Ashley Finger, David Regesch, Jan Sendler, Thomas Paul Weiss, and Tobias Bertram. What is the bandgap of kesterite? *Solar Energy Materials and Solar Cells*, 158:126–129, 2016.

[39] Teodor K Todorov, Jiang Tang, Santanu Bag, Oki Gunawan, Tayfun Gokmen, Yu Zhu, and David B Mitzi. Beyond 11% efficiency: characteristics of state-of-the-art $Cu_2ZnSn(S, Se)\ _4$ solar cells. *Advanced Energy Materials*, 3(1):34–38, 2013.

[40] Christoph Krämmer, Christian Huber, Thomas Schnabel, Christian Zimmermann, Mario Lang, Erik Ahlswede, Heinz Kalt, and Michael Hetterich. Order-disorder related band gap changes in $Cu_2ZnSn(S, Se)\ _4$: Impact on solar cell performance. In *Photovoltaic Specialist Conference (PVSC), 2015 IEEE 42nd*, pages 1–4. IEEE, 2015.

[41] XX Liu and JR Sites. Solar-cell collection efficiency and its variation with voltage. *Journal of Applied Physics*, 75(1):577–581, 1994.

[42] Talia Gershon, Kasra Sardashti, Oki Gunawan, Ravin Mankad, Saurabh Singh, Yun Seog Lee, John A Ott, Andrew Kummel, and Richard Haight. Photovoltaic device with over 5% efficiency based on an n-type $Ag_2ZnSnSe_4$ absorber. *Advanced Energy Materials*, 6(22), 2016.

[43] Marie Buffière, Guy Brammertz, Abdel-Aziz El Mel, Nicolas Barreau, Marc Meuris, and Jef Poortmans. Effect of ammonium sulfide treatments on the surface properties of $Cu_2ZnSnSe_4$ thin films. *Thin Solid Films*, 2016.

[44] Bart Vermang, Viktor Fjällström, Jonas Pettersson, Pedro Salomé, and Marika Edoff. Development of rear surface passivated $Cu(In,Ga)Se_2$ thin film solar cells with nano-sized local rear point contacts. *Solar Energy Materials and Solar Cells*, 117:505–511, 2013.

[45] Samaneh Ranjbar, Guy Brammertz, Bart Vermang, Afshin Hadipour, Shuren Cong, Katsuaki Suganuma, Thomas Schnabel, Marc Meuris, AF da Cunha, and Jef Poortmans. Improvement of kesterite solar cell performance by solution synthesized MoO_3 interfacial layer. *physica status solidi (a)*, 2016.

[46] Bart Vermang, Yi Ren, Olivier Donzel-Gargand, Christopher Frisk, Jonathan Joel, Pedro Salomé, Jérôme Borme, Sascha Sadewasser, Charlotte Platzer-Björkman, and Marika Edoff. Rear surface optimization of CZTS solar cells by use of a passivation layer with nanosized point openings. *IEEE Journal of Photovoltaics*, 6(1):332–336, 2016.

[47] W-W Hsu, JY Chen, T-H Cheng, SC Lu, W-S Ho, Y-Y Chen, Y-J Chien, and CW Liu. Surface passivation of Cu (In, Ga) Se_2 using atomic layer deposited Al_2O_3. *Applied Physics Letters*, 100(2):023508, 2012.

[48] ML Huang, YC Chang, CH Chang, YJ Lee, P Chang, J Kwo, TB Wu, and M Hong. Surface passivation of III-V compound semiconductors using atomic-layer-deposition-grown Al_2O_3. *Applied Physics Letters*, 87(25):252104, 2005.

[49] Jonathan R Bakke, Katie L Pickrahn, Thomas P Brennan, and Stacey F Bent. Nanoengineering and interfacial engineering of photovoltaics by atomic layer deposition. *Nanoscale*, 3(9):3482–3508, 2011.

[50] Jisook Oh, Jihyun Myoung, Jin Sung Bae, and Sangwoo Lim. Etch behavior of ALD Al_2O_3 on HfSiO and HfSiON stacks in acidic and basic etchants. *Journal of The Electrochemical Society*, 158(4):D217–D222, 2011.